

Improving the estimation of thermospheric neutral density via two-step assimilation of in-situ neutral density into a numerical model

Armin Corbin (✉ corbin@geod.uni-bonn.de)

University of Bonn: Rheinische Friedrich-Wilhelms-Universität Bonn <https://orcid.org/0000-0002-6256-0949>

Jürgen Kusche

University of Bonn: Rheinische Friedrich-Wilhelms-Universität Bonn

Research Article

Keywords: thermosphere, neutral mass density, data assimilation, geomagnetic storm

Posted Date: May 11th, 2022

DOI: <https://doi.org/10.21203/rs.3.rs-1616740/v1>

License:   This work is licensed under a Creative Commons Attribution 4.0 International License.

[Read Full License](#)

1 **Improving the estimation of thermospheric neutral density via**
2 **two-step assimilation of in-situ neutral density into a numerical**
3 **model**

4 Armin Corbin, Institute of Geodesy and Geoinformation, University of Bonn, Nussallee 17,
53115 Bonn, Germany, corresponding author, corbin@geod.uni-bonn.de

Jürgen Kusche, Institute of Geodesy and Geoinformation, University of Bonn, Nussallee 17,
53115 Bonn, Germany

6 **Abstract**

7 Neutral thermospheric density is an essential quantity required for precise orbit determination of
8 satellites, collision avoidance of satellites, re-entry prediction of satellites or space debris, and satellite
9 lifetime assessments. Empirical models of the thermosphere fail to provide sufficient estimates of
10 neutral thermospheric density along the orbits of satellites by reason of approximations, assumptions
11 and a limited temporal resolution. At high solar activity these estimates can be off by 70% when
12 comparing to observations at 12 hourly averages. Nowadays, neutral density is regularly observed with
13 satellite accelerometers on board of low Earth orbiting satellites like CHAMP, GOCE, GRACE,
14 GRACE-FO, or Swarm. When assimilating such along-track information into global models of
15 thermosphere-ionosphere dynamics, it has been often observed that only a very local subdomain of the
16 model grid around the satellite's position is updated. To extend the impact to the entire model domain
17 we suggest a new two-step approach: We use accelerometer derived neutral densities from the CHAMP
18 mission in a first step to calibrate an empirical thermosphere density model (NRLMSIS 2.0). In a
19 second step, we assimilate—for the first time—densities predicted for a regular three dimensional grid
20 into the TIE-GCM (Thermosphere Ionosphere Electrodynamics General Circulation Model). Data
21 assimilation is performed using the Local Error-Subspace Transform Kalman Filter provided by the
22 Parallel Data Assimilation Framework (PDAF). We test the new approach using a two week long period
23 containing the 5 April 2010 Geomagnetic storm. Accelerometer derived neutral densities from the
24 GRACE mission are used for additional evaluation. We demonstrate that the two-step approach
25 globally improves the simulation of thermospheric density. We were not able to improve the density
26 prediction at altitudes higher than about 350 km, but we could significantly improve the prediction at
27 the altitude of CHAMP. In fact, the offset between the accelerometer derived densities and the model
28 prediction is reduced by two orders of magnitude when applying the two-step approach. The
29 implication is that our approach allows one to much better 'transplant' the precise CHAMP
30 thermospheric density measurements to satellites flying at a similar altitude.

31 **Keywords**

32 thermosphere, neutral mass density, data assimilation, geomagnetic storm

33 **Background**

34 Neutral thermospheric density plays an important role when computing the atmospheric drag acceleration
35 acting on satellites (e.g., Vallado and Finkleman, 2014). Applications in need for accurate drag estimates
36 are precise orbit determination (e.g., Montenbruck and Gill, 2005; Longuski, Hoots, and Pollock IV,
37 2022), the forecasting of orbit decay or mission life time (e.g., Walterscheid, 1989), and predicting the
38 re-entry of satellites or space debris and identifying locations on Earth that might be endangered by this
39 (e.g., Klinkrad et al., 2006). Especially, satellites flying below 1000 km are affected by atmospheric drag
40 that is the largest non-gravitational acceleration at those altitudes.

41 One can determine the neutral density with different methods (Emmert, 2015). In-situ measurements
42 are conducted with mass spectrometers or accelerometers mounted on satellites. However, there are only
43 a few satellites equipped with such instruments. It is also possible to estimate time averaged neutral
44 densities from observed satellite orbits. The advantage of this method is that it can be applied to any
45 passive satellite, but it is less accurate when relying on two line elements (TLE) tracking. In case of
46 active satellites—for example, satellites equipped with retro reflectors for satellite laser ranging—the
47 time averaged neutral density can be determined within precise orbit determination with higher precision
48 than using TLE.

49 Another approach is the use of thermospheric density models. In fact, several numerical and empirical
50 models were developed over the last seven decades (e.g., Doornbos (2012, Table 2.1) and Vallado and
51 Finkleman (2014, Figure 3)). Empirical density models are constructed from observations that are fitted
52 to mathematical equations. This is in particular critical for the effect of solar and geomagnetic forcing
53 on density, since the underlying physics including Joule heating, photochemistry, particle precipitation
54 is partly not understood and partly too complex for these simple equations, and one is missing also
55 important data. Empirical density models represent the average state of the atmosphere (e.g., Emmert,
56 2015). Examples for empirical models are the Jacchia-Bowman (JB, Bowman et al., 2008) model, Naval
57 Research Laboratory Mass Spectrometer and Incoherent Scatter radar (NRLMSIS 2.0, Emmert et al.,
58 2021) model, and Drag Temperature Model (DTM, Bruinsma and Boniface, 2021).

59 Numerical models propagate an initial state using physical laws and principles, for instance, heat and
60 momentum balance, electromagnetism and chemical reactions. Typically, this is done by solving a set
61 of (partial) differential equations on a grid. Examples for numerical models are the National Center for
62 Atmospheric Research Thermosphere Ionosphere Electrodynamics General Circulation Model (NCAR

63 TIE-GCM, Qian et al., 2014), NCAR Whole Atmosphere Community Climate Model (WACCM-X, Liu
64 et al., 2018), and Global Ionosphere–Thermosphere Model (GITM, Ridley, Deng, and Tóth, 2006).

65 There are significant discrepancies between different models, and between models and observations (e.g.,
66 Gaposchkin and Coster, 1990; Bruinsma, Sean L. et al., 2012; Bruinsma, Doornbos, and Bowman, 2014;
67 He et al., 2018; Panzetta et al., 2019). Hence, there is an ongoing effort in improving the models. In this
68 paper we present a new experimental approach for that purpose.

69 While numerical models provide physically consistent solutions, they do not exhibit improved skills
70 in neutral density simulation when compared to empirical models (e.g., Emmert, 2015). A common
71 approach to nudge numerical model simulations closer to reality is merging them with observations via
72 data assimilation.

73 In a coupled model, like the TIE-GCM, assimilating quantities associated with a compartment also
74 affects the other compartments. One can assimilate observations of the electron density to improve the
75 representation of the neutral mass density. For example, the total electron content, an integrated measure
76 of electrons along a path through the atmosphere, could be used for that. Although we only assimilate
77 neutral mass densities here, our approach is set up in a way to allow the assimilation of other quantities.
78 The in-situ measurements of a single satellite mission only intersect with a small subset of the model grid
79 cells. This means, compared with models the in-situ measurements of a single satellite are very sparse.
80 The farther an observation is away from a grid cell, the less information is provided by it for that cell.
81 For instance, a measurement of the neutral density on the day side provides little information about
82 the density on the night side. Thus, assimilating such along track data should only affect grid cells in
83 the vicinity of the satellite’s orbit. Matsuo, Lee, and Anderson (2013) have assimilated neutral densities
84 derived from the CHAMP (Reigber, Lühr, and Schwintzer, 2002) accelerometer into the TIE-GCM. The
85 model densities were only improved in the vicinity of the satellite’s orbit. But they achieved global
86 improvements by co estimation of model drivers.

87 Besides co estimating parameters for the model drivers, one could also assimilate data of many sources at
88 different locations simultaneously for global model improvements. In this study we test another approach
89 that consists of two steps and is illustrated in Figure 1. We use the along track densities derived from the
90 CHAMP accelerometer to calibrate an empirical model (the NRLMSIS 2.0). The calibrated empirical
91 model is viewed here as a combination of the data used to build the empirical model itself and the densities
92 derived from the CHAMP accelerometer, with more weight given to the CHAMP observations. For the

93 calibration we evaluate the empirical model along the CHAMP orbit and scale the observed densities by
94 the modeled densities to derive scale factors. We also apply a low pass filter to the scale factors. The
95 calibrated model is the output of the original model multiplied with the corresponding scale factor. In
96 the first step, we evaluate the calibrated empirical model on a regular three dimensional grid. We call it
97 the *data grid*. In the second step, we assimilated the data located on the *data grid* into the TIE-GCM
98 that is located on what we call the *state grid*.

99 Data assimilation (e.g., Lahoz, Khattatov, and Menard, 2010) combines the state estimate of a model
100 with observations taking into account the uncertainty of both to get an estimate of the state with higher
101 accuracy. There are many different data assimilation approaches. However, for large scale problems, like
102 atmosphere models, ensemble Kalman filters (e.g., Vetra-Carvalho et al., 2018) are frequently employed.
103 By representing the variance covariance matrix of the model state implicitly with an ensemble of states,
104 they are very efficient w.r.t. computational costs and computer memory requirements, and easy to
105 integrate into model code. These filters utilize a sequence of *forecast* and *analysis* steps. The forecast
106 step uses the model to predict the observations at time t_i . At the subsequent analysis step the state
107 of the model is fitted so that it minimizes the distance to the forecasted observations and the actual
108 observations w.r.t. the associated variance co-variance matrices.

109 The Parallel Data Assimilation Framework (Nerger, Tang, and Mu, 2020) developed at the Alfred Wegener
110 Institute Bremerhaven is open-source software for ensemble based data assimilation. It is designed for
111 large scale numerical models and allows the application of different filter algorithms. Moreover, it enables
112 parallel computation of all ensemble members, which in turn can also be calculated in parallel if supported
113 by the model. Both, the TIE-GCM and PDAF are written in Fortran which simplifies the implementation.
114 In this study we use the localized (Nerger et al., 2006) error-subspace transform Kalman filter (ESTKF)
115 (Nerger et al., 2012b).

116 Given the atmospheric drag acting on a satellite, together with a model describing the shape and
117 material of the satellite one can derive the neutral mass density at the satellite's position (e.g., Doornbos,
118 2012, p.91). Since accelerometers aboard satellites measure the superposition of all non conservative
119 accelerations acting on the satellite, one must first reduce the measurements to obtain the atmospheric
120 drag. To this end, one needs to model the acceleration caused by solar radiation pressure and Earth
121 radiation pressure, and remove it from the the measured accelerations. For this study, we use the neutral
122 mass densities derived from the accelerometers on board of the CHAMP (Reigber, Lühr, and Schwintzer,

123 2002) and GRACE (Tapley et al., 2007) mission using the approach described in Vielberg et al. (2018)
124 and Vielberg and Kusche (2020). Further information can be found at Vielberg et al. (2021).

125 The NCAR Thermosphere Ionosphere Electrodynamics General Circulation Model (TIE-GCM, Qian et
126 al., 2014), represents a global, numerical model of the upper atmosphere. The TIE-GCM ranges from
127 approximately 97 km to 500 km altitude. The upper boundary is not fixed in geometric height coordinates,
128 since the TIE-GCM uses pressure levels as vertical coordinate. For this study we use the latest version
129 of the TIE-GCM (version 2.0). An important proxy driver for the TIE-GCM is the F10.7 index (e.g.,
130 Tapping, 2013) that is used to compute the extreme ultraviolet (EUV) radiation, based on the model
131 of Richards, Fennelly, and Torr (1994). The TIE-GCM includes two alternative empirical high-latitude
132 potential models computing ionospheric convection: The Heelis model (Heelis, Lowell, and Spiro, 1982)
133 and the Weimer model (Weimer, 2005). The first requires the three hourly Kp index (e.g., Matzka et al.,
134 2021), whereas the second uses solar wind and interplanetary magnetic field parameters provided by the
135 OMNI Dataset with one minute temporal resolution (Papitashvili and King, 2020).

136 The Naval Research Laboratory Mass Spectrometer Incoherent Scatter radar 2.0 (NRLMSIS 2.0, Emmert
137 et al., 2021) model is a global, empirical model of the atmosphere. It takes location, time, geomagnetic
138 activity represented by the Kp index, and solar activity represented by the F10.7 index as input. It
139 computes the neutral composition, density, and temperature. Since it is derived from various observations
140 at different periods and locations the results represent the averaged observed state of the atmosphere for
141 the given inputs. The model extends from the ground to the exobase.

142 Data assimilation of various observations types has already been applied to different models of the upper
143 atmosphere in several studies: Solomentsev et al. (2012) have assimilated simulated GPS observations
144 into a numerical model of the ionosphere using the Ensemble Square Root Filter. The aim was assessing
145 the state estimation of the ionosphere and improving the estimation of model drivers. Observations from
146 GPS Occultation have been assimilated by Lee et al. (2012) into the TIE-GCM using the Ensemble
147 Kalman filter under geomagnetic quiet conditions. They aimed at improving the global ionospheric
148 electron density specification. Matsuo, Lee, and Anderson (2013) have assimilated CHAMP observations
149 and GPS Occultation measurements into the TIE-GCM using the Ensemble Kalman filter. They found
150 that assimilation of accelerometer derived densities only improves the model densities in the vicinity
151 of the satellite's orbit. But they also demonstrated that co estimating the F10.7 parameter together
152 with accelerometer derived densities impacts the global model. In the study of Morozov et al. (2013)

153 the ensemble adjustment Kalman filter is used to assimilate CHAMP observations into the Global
154 Ionosphere–Thermosphere Model during a geomagnetically calm period. They estimate the F10.7 index in
155 a way it has a constant variance. They could reduce the model bias along the CHAMP and GRACE orbits.
156 Codrescu, Codrescu, and Fedrizzi (2018) have assimilated neutral densities derived from accelerometers
157 on board of the CHAMP mission into the CTIPe model during quiet conditions at solar minimum using
158 the Ensemble Kalman Filter. The model results were improved when comparing to CHAMP and GRACE
159 observations. Forootan et al. (2022) have applied a calibration and data assimilation technique to the
160 empirical NRLMSISE-00 model using observations from the GRACE accelerometer.

161 **Methods**

162 **Period for Experiments**

163 The period of the assimilation experiment is restricted by three factors: First, it must contain mea-
164 surements of the CHAMP and GRACE missions. That is, the period must be between 2002 and 2010.
165 Second, the period must contain at least one strong storm ($K_p \geq 7$), but also quiet condition, so we can
166 evaluate the assimilation framework for different geomagnetic activity. Finally, the duration is restricted
167 by the computing time. A two week long period is processed on our hardware (400 cores distributed over
168 25 Intel(R) Xeon(R) Gold 6130 processors) in about four hours and 20 minutes. This allows us to test
169 different settings in a reasonable amount of time. We choose the period from 27 Mar 2010 00:00 UTC+0
170 till 10 April 2010 00:00 UTC+0, that satisfies all three conditions. In Figure 2 the solar and geomagnetic
171 activity during the experiments is illustrated. On April 5, 2010, an interplanetary coronal mass injection
172 reached Earth around 8:27h UTC+0 and triggered a geomagnetic storm (Lu et al., 2014; Sheng et al.,
173 2017). The mean altitudes of the CHAMP and GRACE satellite during the experiment are 302 km and
174 474 km, respectively.

175 **Calibration of NRLMSIS 2.0**

176 The majority of the observations used to estimate the NRLMSIS 2.0 parameters are between the ground
177 and 105 km altitude (Emmert et al., 2021, Table 1). Above this altitude only density observations
178 derived from two line elements were used along with synthetic observations from the preceding model
179 NRLMSISE-00. Since, the TIE-GCM starts at approximately 97 km altitude it does not intersect with
180 most of the observations used for building the NRLMSIS 2.0. Moreover, empirical models return average
181 states of the atmosphere. Thus, we calibrate the model to perform better at the altitudes covered by the

182 TIE-GCM.

183 We calibrate the NRLMSIS 2.0 by scaling it with time dependent factors. The scale factor is thus defined
184 as the quotient of the density derived from the CHAMP accelerometer and the density predicted by the
185 NRLMSIS 2.0 for the corresponding location and time. In Figure 3 the scale factors for the duration of
186 the experiment are plotted. During and after the strong storm (starting at 5th April) the scale factors are
187 much larger compared to the rest of the period (Figure 3 a and c). Within each orbit, the scale factors
188 vary according to latitude and whether the satellite is on the day or night side (Figure 3 b). For example,
189 on the night side equator (argument of latitude is zero) the scale factors are systematically larger than on
190 the day side equator (argument of latitude is 180°). The median scale factor on the night side is about
191 16% larger than the median on the day side.

192 As shown, the scale factor depends on the horizontal location. However, for each epoch, we can only
193 derive the scale factor at one location if we use only one satellite. That is, the scale factor is expected to
194 work best for locations near the CHAMP satellite.

195 Thus, we decided to filter out the orbital signal in the scale factor time series. We found that a cut-off
196 frequency of three hours, which approximately corresponds to two revolutions of the CHAMP satellite,
197 eliminates this signal (see Figure 3 d and e). That is, the variability between day and night side within an
198 orbit vanishes in the filtered scale factor time series. The three hourly filtered scale factor is an average
199 value that can be applied to the whole model, at the cost of signal loss (compare Figure 3 a and d).
200 Consequently, the cut-off frequency also limits the duration between subsequent analysis steps.

201 As shown in Zeitler et al. (2021) half daily scale factors derived at different heights are highly correlated.
202 For CHAMP and GRACE the correlation is 89%. Thus, when calibrating the NRLMSIS 2.0 with
203 observations from the CHAMP mission, we expect that the calibrated model also fits better to the
204 densities derived from the GRACE accelerometer.

205 **Spatial Resolution of the Data Grid**

206 We choose the horizontal resolution of the *data grid*, so that it reflects the resolution of the NRLMSIS 2.0.
207 The NRLMSIS 2.0 uses spherical harmonics up to degree six to expand the model parameters to the
208 global atmosphere (Hedin (1987, Equation A22) and Emmert et al. (2021, Section 2.4)). That is, the
209 NRLMSIS 2.0 cannot resolve signals with wavelength smaller than $\frac{360^\circ}{6} = 60^\circ$ arc length. To sample
210 these signals, one needs at least half the wavelength. Here, we choose a third which gives 20° for the
211 horizontal resolution of the *data grid*. Using a finer grid would increase the number of observations and

212 slow down the assimilation while the gain in information is limited. The *data grid* starts at 100 km and
213 ends at 550 km covering most of the *state grid*. The vertical resolution is 25 km. This value corresponds
214 approximately to the number density scale height at 200 km altitude.

215 **Setup for TIE-GCM**

216 We use the latest version of the TIE-GCM (version 2.0). The TIE-GCM either runs with 5.0° or 2.5°
217 horizontal resolution. For this study, we use the coarser five degree resolution since it runs about ten
218 times faster and requires one eighth of the disk space to store the results at the same temporal resolution.
219 The step size—the time between subsequent model states—is 15 seconds. We found it difficult to use
220 longer values as this caused some ensemble members to crash. We do not save every model step, since it
221 would require too much memory: Saving the ensemble mean of the neutral density at the *state grid* at
222 each model step for a two week long period using single precision requires approximately 24 GB. But we
223 also need to save the data at the *data grid* and the corresponding standard deviations. If one also stores
224 the results of each ensemble member the storage requirements increase accordingly. Thus, we save the
225 results every ten minutes.

226 The TIE-GCM requires lower boundary constraints for neutral temperature, horizontal neutral wind,
227 and geopotential altitude. By default a 'flat' lower boundary is assumed. That is, there is no wind,
228 the neutral temperature is 181 K, and the geopotential height is 96.4 km. Alternatively, one can use
229 zonal monthly mean climatologies to specify the lower boundaries. This feature is based on the work of
230 Jones Jr. et al. (2014). The TIE-GCM comes with a file containing zonal climatologies derived from the
231 NRLMSISE-00 (Picone et al., 2002) and the Horizontal Wind Model (HWM07, Drob et al., 2008). To
232 use it with the five degree grid one has to interpolate, since it is only given for the 2.5 degree grid. The
233 migrating diurnal and semi-diurnal tides at the lower boundary are provided by the Global Scale Wave
234 Model 2002 (GSWM-02 Hagan and Forbes, 2002).

235 **Ensemble Generation**

236 We create the ensemble by adding perturbations to the external forcing, lower boundary conditions
237 and some constants to each ensemble member that are sampled from a truncated multivariate normal
238 distribution with zero mean. The truncation of the normal distribution is necessary to prevent model
239 crashes caused by extreme values sampled from the tails of the normal distribution that are invalid or
240 unrealistic. We sample the perturbations once and use the same values for the entire duration of the
241 experiment. For each lower boundary condition, only one value is sampled, which is added to all elements

Table 1. The quantities that are perturbed to generate the ensemble are listed in the first column. The solar wind parameters are only perturbed if the Weimer model is used. Whereas hemispheric power and cross tail potential are only perturbed in case of the Heelis model. The last two columns are the parameters used for sampling the truncated normal distributions. The mean is always zero. Note that correlations are not listed in this table. The truncation is symmetric. That means values larger than the positive truncation threshold as well as values less than the negative truncation threshold are rejected.

	units	standard deviation	truncation
external forcing			
F10.7	sfu	1	± 50
hemispheric power	GW	5	± 9
cross tail potential	kV	8	± 12
solar wind density	$\frac{1}{\text{cm}^3}$	0.1	± 0.3
solar wind velocity	$\frac{\text{km}}{\text{h}}$	45	± 135
lower boundary conditions			
neutral temperature	K	3	± 9
neutral zonal wind	$\frac{\text{cm}}{\text{s}}$	500	± 1500
neutral meridional wind	$\frac{\text{cm}}{\text{s}}$	650	± 1950
geopotential height	cm	7000	± 21000
constants			
Characteristic Maxwellian energy of polar cusp electrons	keV	0.01	± 0.03
Characteristic Maxwellian energy of drizzle electrons	keV	0.05	± 0.15
Joule heating factor	-	0.15	± 0.45

242 of the corresponding field. We do not consider errors within the field, but a global offset of the lower
 243 boundary condition. In Table 1 the parameters of the probability density function are listed.

244 Since we have no access to the true probability density function of the perturbed parameters, we have
 245 to determine it to a certain extend arbitrarily. The standard deviation of the constants that we perturb

246 is assumed to be 10% of the constant itself. Following Tapping (2013) we assume that the standard
 247 deviation of the F10.7 index is one solar flux unit for values smaller than 100. When using the Heelis
 248 model we perturb hemispheric power and cross tail potential. Since both are computed within the TIE-
 249 GCM from the Kp index we introduce a correlation of 0.9. If the Weimer model is employed, we perturb
 250 the solar wind velocity and density instead. The constant lower boundary conditions of the TIE-GCM
 251 are perturbed by diurnal and semi-diurnal tides computed by the global scale wave model (GSWM). We
 252 decided to approximate the standard deviation of the lower boundary conditions from the GSWM tidal
 253 perturbations. We take 10% of the largest absolute tidal perturbation in March.
 254 We use an ensemble with 100 members. The initial value for the assimilation are computed with an open
 255 loop simulation, which starts ten days before the assimilation experiment.

256 State Vector and Observation Operator

The TIE-GCM approximates the state of the atmosphere at an epoch with multiple quantities located
 on the *state grid*, given for the current and previous model step. The neutral mass density can be linked
 to these fields via the mass fractions w of the modeled species and the neutral temperature T . Thus, in
 our the study the state vector is composed of

$$\mathbf{x} = [\mathbf{T}, \mathbf{T}', \mathbf{w}_O, \mathbf{w}'_O, \mathbf{w}_{O_2}, \mathbf{w}'_{O_2}, \mathbf{w}_{He}, \mathbf{w}'_{He}]. \quad (1)$$

257 O, O₂, He denote atomic Oxygen, molecular Oxygen and atomic Helium, respectively. The quantities
 258 evaluated at the previous step are denoted with a prime symbol.

The observation operator H is a composition of the function computing the neutral mass density $\rho(\mathbf{x})$
 and an interpolation function $I()$ that computes the values at the *data grid* given values on the *state grid*:

$$\mathbf{y} = H(\mathbf{x}) = (I \circ \rho)(\mathbf{x}) \quad (2)$$

For each cell of the *state grid* and each step, we can compute the neutral mass density assuming an ideal
 gas with

$$\rho = \frac{p\bar{M}(w_O, w_{O_2}, w_{He})}{RT}. \quad (3)$$

Here, p is the pressure, R denotes the gas constant and \bar{M} is the mean molar mass

$$\bar{M}(w_O, w_{O_2}, w_{He}) = \frac{1}{\frac{w_O}{M_O} + \frac{w_{O_2}}{M_{O_2}} + \frac{w_{He}}{M_{He}} + \frac{w_{N_2}}{M_{N_2}}} \quad (4)$$

259 The molar mass of a species is denoted with M , and the mass fraction of molecular Nitrogen is
 260 $w_{N_2} = 1 - w_O - w_{O_2} - w_{He}$.

261 Since the *state grid* is irregularly spaced in the vertical dimension, we first perform linear interpolation
 262 along this axis. Since the neutral mass density decreases almost exponentially with height, we apply
 263 the natural logarithm to the neutral densities before performing the vertical interpolation. This ensures
 264 small interpolation and especially small extrapolation errors, since on a logarithmic scale the density
 265 profiles are almost linear. We then apply the exponential function to the vertically interpolated values to
 266 transform the interpolated values back to neutral mass densities. Two more linear interpolations along
 267 the horizontal coordinates axes are performed to compute the mass densities on the *data grid*. If the
 268 observations are given exactly at the time of the current step, another interpolation along the time axis
 269 is not necessary.

270 Observations

271 At each analysis step we assimilate the neutral mass densities from the calibrated NRLMSIS 2.0 located
 272 on the *data grid* into the TIE-GCM. The current implementation only supports uncorrelated observation.
 273 Thus, although the observations are highly correlated we cannot account for it by using the full variance
 274 covariance matrix of the observations.

We approximate the standard deviation of the NRLMSIS 2.0 neutral mass density by multiplying the uncalibrated neutral mass density ρ with a factor f_h depending on the altitude. The height dependent factor is obtained from the standard deviations provided in (Emmert et al., 2021, Data Set 5) for the epoch 2006-2013 at 250 km and 400 km altitude. We use linear interpolation to get the standard deviation for arbitrary heights:

$$f_h(h) = \begin{cases} 0.148 + \frac{h - 250}{1500} & h < 400 \text{ km} \\ 0.248 + \frac{h - 400}{3260} & h \geq 400 \text{ km} \end{cases} \quad (5)$$

We introduce additional weights: $p_{\text{ga}}(\text{Kp})$, $p_{\text{dist}}(d)$, and p_0 to account for the geomagnetic activity, the distance to the CHAMP satellite and a constant factor, respectively. The standard deviation is computed with

$$\sigma_\rho(\rho, h, \text{Kp}, d) = f_h(h) \rho \frac{1}{p_{\text{ga}}(\text{Kp})} \frac{1}{p_{\text{dist}}(d)} \frac{1}{p_0} \quad (6)$$

We use the Kp index as indicator of the geomagnetic activity. For quiet periods ($\text{Kp} < 4\frac{2}{3}$) the weight is one. For the maximal Kp value of 9, the factor is $\frac{1}{2}$. The values in between are linearly interpolated.

This factor ensures that the NRLMSIS 2.0 observations have a lower weight during storms.

$$p_{\text{ga}}(\text{Kp}) = \begin{cases} 1 & \text{Kp} < 4\frac{2}{3} \\ \frac{40 - 3 \text{Kp}}{26} & \text{Kp} \geq 4\frac{2}{3} \end{cases} \quad (7)$$

The standard deviation is weighted by the distance between the CHAMP satellite and the center of the corresponding *data grid* cell. We use two exponential decay functions depending on the spherical distance Δ_ϕ on the unit sphere and the vertical geocentric distance Δ_h .

$$p_{\text{dist}}(\Delta_\phi, \Delta_h) = \exp\left(-\frac{\ln(2)}{\Lambda_\phi} \Delta_\phi\right) \exp\left(-\frac{\ln(2)}{\Lambda_h} |\Delta_h|\right) \quad (8)$$

275 The weighting is controlled by the half life parameters Λ_ϕ and Λ_h . For the experiments presented in this
276 study Δ_ϕ is infinite. That is, the spherical distance has no impact on the weights.

277 **Forecast Duration**

278 The forecast duration is the duration between two subsequent analysis steps. If the forecast duration
279 is too long, it will resemble the open loop simulation some time before the next analysis step. If it
280 is too short, the assimilated data might be reproduced. In that case the assimilation is useless since
281 one could use the assimilated data directly. For this consideration also the standard deviation of the
282 observations and the model forecast are important. If the observations have much larger uncertainties
283 than the forecast, the result resembles the open loop simulation and the other way round.

284 The lower bound of the forecast duration is given by the model step length. The forecast duration should
285 not exceed the cut-off period of the low pass filter applied to the scale factors.

286 The model step length is 15 seconds and the NRLMSIS 2.0 has been filtered with a three hourly low pass
287 filter. Thus, we choose to perform the analysis step hourly.

288 **Localization**

289 At each analysis step of a global filter, each element of the state vector is updated taking into account
290 all observations, regardless how far the observations are away from the location of the corresponding
291 element of the state vector. This can be of advantage if there are long-range correlation in the system
292 (e.g., the ocean or the atmosphere). For instance, a single in-situ observation within the atmosphere could
293 theoretically improve the state estimate of the whole atmosphere. However, this requires that significant
294 long-range correlations exist and that they are correctly represented by the ensemble. Typically, the
295 random errors in the representation of the covariances are larger than the actual signal for small ensembles
296 (Nerger et al., 2006, p.640). This can lead to spurious correlations (e.g., Hamill, Whitaker, and Snyder,

297 2001) and locally incredible estimates (Nerger et al., 2006, p.640). This problem is addressed by filtering
298 out long-range correlations in the analysis step by applying localization (e.g., Nerger et al., 2012a).

299 For the ESTKF, domain localization (Nerger et al., 2006) together with an optional observation localiza-
300 tion (Hunt, Kostelich, and Szunyogh, 2007) is implemented within PDAF: The *state grid* is subdivided
301 into disjoint sub-domains. Only observations whose distance from the center of the corresponding sub-
302 domain is smaller than a cut-off radius are used to update the elements of the state vector within the
303 sub-domain.

304 The geometric horizontal extent of the *state grid* cells and *data grid* cells increases with altitude. An
305 edge at 550 km altitude is 7% larger than at 100 km. Moreover, the vertices of each grid are located
306 closer to each other at the poles. At the equator the distance between two neighbouring vertices along a
307 circle of latitude is almost six times larger than at 80° latitude. Additionally, the vertical extent of the
308 *state grid* cells increases with altitude due to the use of pressure levels. To include about the same number
309 of observations at each sub-domain, we compute the distance using the indices of the *state grid* cells as
310 coordinates. To transfer the coordinates of the *data grid* to the index coordinates of the *state grid*, we
311 use the geometric height of the ensemble mean.

312 We subdivided the *state grid* into sub-domains containing at most three cells in meridional, zonal and
313 vertical direction. The distance is computed using the L2 norm. The cut-off radius is seven grid cells.

314 Additionally, we apply observation localization in some experiments. For each sub-domain the associated
315 observations are weighted based on the distance. PDAF computes the weights with a finite function
316 that mimics a Gaussian, realized as polynomial of order five (Gaspari and Cohn, 1999, Eq. 4.10). This
317 weighting function monotonically decreases from one at zero distance to zero at a distance equal to the
318 cut-off radius.

319 **State Constraints**

320 After the update step the state vector may contain values that are physically impossible. Thus, we enforce
321 the following constraints:

- 322 • The neutral temperatures given in Kelvin must be positive.
- 323 • The mass fraction of each species must be in the interval $[0, 1]$.
- 324 • The mass fractions at each location must sum up to one.

experiment identifier	OLS 1	OLS 2	OLS 3
high-latitude potential model	Heelis	Heelis	Weimer
lower boundary	flat	MSIS & HWM	MSIS & HWM

Table 2. Setup for open loop simulations. Only settings that differ are listed.

325 Results and Discussion

326 Open-loop Experiments

327 At first we try different setups for the TIE-GCM without assimilating any data. We investigate two setups
328 for the lower boundary conditions: A flat lower boundary and a zonal mean climatology lower boundary
329 derived from the MSIS and HWM. Additionally, we compare open loop simulations using the Heelis and
330 Weimer model. The open loop experiments are summarized in Table 2. The following discussion always
331 refers to the ensemble mean of the open loop experiments.

332 When using the zonal mean climatology instead of a flat lower boundary the median density along the
333 CHAMP orbit increases by 5% (OLS 2 vs. OLS 1). When using the Weimer model instead of the Heelis
334 model the median density along the CHAMP orbit increases by 10% (OLS 3 vs. OLS 2). The along
335 track densities of OLS 1 and OLS 2 show the same behaviour and are basically separated by an offset,
336 whereas the along track densities of OLS 3 have other features (see Figure 4). Especially in the vicinity
337 of the poles, the densities associated with OLS 3 match better to the course of the accelerometer derived
338 densities (e.g., GRACE at 20:30 in Figure 4).

339 The height profiles showing the average neutral density in Figure 5 associated with the TIE-GCM intersect
340 with the profiles associated with the NRLMSIS 2.0. The height of the intersection is different for each
341 open loop simulation (see horizontal dotted lines). The average density of all TIE-GCM open loop
342 simulations below the intersections is higher than the average density of the NRLMSIS 2.0. Accordingly,
343 above the intersections the NRLMSIS 2.0 has higher densities. This means that at the analysis steps, the
344 densities above the corresponding intersection must increase, while the densities below must decrease. In
345 other words, the innovation has a different sign depending on the altitude.

346 Data Assimilation Experiments

347 We tested different setups for the data assimilation that are summarized in Table 3. For the TIE-GCM we
348 use the same setup as for the OLS 3, since the external forcing has the highest temporal resolution. We

Table 3. Setups for the data assimilation experiments. A 'completion' of 100% means that the experiment ran to the end without any errors. Values below 100% indicate that the TIE-GCM crashed after the corresponding percentage of the experiment's intended duration. 'median difference' refers to the median of the differences between ensemble mean and accelerometer derived density of the corresponding satellite.

ID	completion	Λ_h (km)	p_0	forget factor	observation localization	median difference ($\frac{\text{g}}{\text{cm}^3}$)	
						CHAMP	GRACE
10	100%	600	3.0	1.00	yes	-5.3e-16	-1.5e-16
11	100%	600	4.0	1.00	yes	-6.4e-16	-1.5e-16
12	100%	100	4.0	1.00	yes	-6.8e-17	-1.5e-16
13	100%	100	4.0	1.00	no	-7.1e-17	-1.3e-16
14	100%	100	1.0	1.00	no	3.7e-16	-1.4e-16
15	100%	100	6.0	1.00	no	4.1e-17	-1.3e-16
16	8%	∞	4.0	0.75	no	-1.0e-17	-1.3e-16
17	54%	∞	2.0	0.90	no	-6.5e-16	-1.5e-16
18	20%	900	2.0	0.85	no	-4.5e-16	-1.3e-16
19	22%	300	3.0	0.85	no	-3.7e-16	-1.3e-16
20	100%	500	4.0	1.00	no	9.0e-17	-1.3e-16
21	80%	500	3.0	0.95	no	-1.8e-16	-1.2e-16
OLS 3	100%					7.3e-15	9.2e-17

349 were able to improve the neutral density predication for the CHAMP satellite, but not for the GRACE
350 satellite, regardless of the setup (see last column of Table 3). Since the overall behaviour is the same for
351 all setups, we show only results from experiment 13 to illustrate that behaviour. We present only the
352 ensemble mean of the neutral densities, since it reduces the dimensionality of the ensemble, simplifying
353 the illustration of the results.

354 We first look at the temporal evolution of the ensemble mean. Figure 6 shows the time series of the
355 neutral mass densities at nine cells of the *data grid* for the first two days of the experiment. The columns
356 contain the time series located at 300 km, 400 km, and 475 km, respectively. The average height during

357 the experiment of the CHAMP and GRACE satellite are 302 km and 474 km, respectively. Thus, the
358 first column is associated with the CHAMP mission and the third column with the GRACE satellite.
359 There is a large correction at the first analysis step. The subsequent corrections are smaller. At the first
360 analysis step (27 March) the neutral density is pulled towards the calibrated NRLMSIS 2.0 in all panels.
361 The innovation is the difference between the densities of the calibrated NRLMSIS 2.0 and the densities
362 forecasted by the model. At 475 km at the equator and at $60^\circ N$ latitude (panels f and c) the magnitude
363 of the correction amounts about twice the innovation. That means the distance between the open loop
364 simulation and the calibrated NRLMSIS 2.0 is as large as the distance between the assimilation run
365 and the NRLMSIS 2.0, but with different sign. This *initial overshooting* remains for the rest of the
366 experiment.

367 Figure 7 illustrates in the same way as Figure 6 neutral density time series, but shows another period
368 including the storm. The corrections are larger than in Figure 6 showing quiet conditions. During the
369 forecast phase the ensemble mean departs much faster from the analysed state as under quiet conditions.
370 Consequently, at the subsequent analysis steps larger corrections are necessary. The analysed state does
371 not fit to the model dynamics during the storm.

372 As suggested by Figure 6, the overshooting depends on the altitude. Figure 8 relates the innovation at
373 each altitude of the *data grid* with the actual correction performed at the analysis step for the first nine
374 analysis steps. Overshooting starts at about 350 km (intersection of the dark blue line with right vertical
375 line). In the following analysis steps the portion of the innovation being adopted further decreases below
376 300 km altitude. This makes sense since the model forecast is much closer to the NRLMSIS 2.0 after the
377 first analysis step at this altitudes. After the first analysis step the ratio becomes negative roughly above
378 350 km, indicating the model is pushed away from NRLMSIS 2.0.

379 In Figure 9 we show the average ratio of the standard deviations of the NRLMSIS 2.0 and the forecasted
380 ensemble at the four first analysis steps. After the first analysis step the standard deviation of the
381 ensemble is drastically reduced, so that the ratio becomes much larger. Especially, at the upper part
382 of the *data grid* the ensemble standard deviation becomes much smaller. Therefore, the innovation is
383 almost ignored at that altitudes (see Figure 8).

384 The difference between the forecast and analysis ensemble mean are shown in Figure 10 on world maps
385 for different pressure levels and analysis steps. The position of CHAMP is marked with a star symbol.
386 The model is updated globally, as expected. At the first analysis step the densities are mainly lowered.

387 A dependency on the location of the satellite is not visible.

388 To compare the neutral densities from the assimilation experiment with the densities derived from the
389 accelerometers, we interpolate the densities on the *state grid* to the corresponding orbits using the same
390 method that is used to interpolate the *state grid* to the *data grid*. In Figure 11 the along track neutral
391 densities are plotted for a twelve hour long subset of the experiment including the storm. The assimilation
392 run fits much better to the observations than the open loop simulation. It also shows more features
393 than the calibrated NRLMSIS 2.0, for example, at 12:20, 15:20, or 16:10. For GRACE, the densities
394 interpolated from the assimilation run are systematically smaller than the calibrated NRLMSIS 2.0 and
395 the open loop simulation.

396 Figure 12 confirms the previous findings. Along the orbit of CHAMP the assimilation run is much closer
397 to the accelerometer derived densities than the open loop simulation. In contrast, along the GRACE
398 orbit the densities associated with the assimilation run are smaller than the observations, whereas the
399 densities from the open loop simulation are larger. The calibrated NRLMSIS 2.0 is closer to the GRACE
400 observations than the uncalibrated model, but the mean difference is not zero, as it is almost the case for
401 CHAMP observations.

402 There are two major issues with our approach: First, none of the setups could improve the density
403 estimation at the altitude of GRACE. The first analysis step pulls the model beyond the observations.
404 The ensemble spread becomes much smaller after the first analysis step, and in the subsequent analysis
405 steps the observations are almost ignored at high altitudes. Second, there are large jumps in the ensemble
406 mean time series during the storm. The model departs from the analysed state much faster as during quiet
407 conditions. We believe that both issue could be reduced by co estimating suitable model parameters,
408 that are not limited to corrections for external forcing, like the F10.7 proxy. For example, one could
409 try corrections for hard coded parameters like chemical reaction rates, eddy diffusion, thermal diffusion,
410 characteristic energy of particles, solar proton flux, but at present we cannot yet provide a specific
411 recommendation. Sheng et al. (2017) suggests that the cooling processes are not correctly represented
412 in the TIE-GCM at the 5 April 2010 geomagnetic storm and Lu et al. (2014) suspects that the eddy
413 diffusion coefficient is too high during the storm.

414 Nevertheless, we could demonstrate that at the altitude of the CHAMP satellite, the offset between the
415 accelerometer derived densities and the ensemble mean vanishes using the two-step approach.

416 There are many options for the data assimilation setup: The ensemble generation, filter choice and related

417 settings, and the calibration of the NRLMSIS 2.0 and the approximation of the standard deviation could
418 be tuned in follow-on research. Within the limitations of this study, we have explored only a small subset.
419 A caveat is that our experiments were conducted in a period with small solar irradiance, and that for
420 a period with high solar activity other settings might be necessary. Moreover, we suggest that further
421 research could focus on adding, additional independent observations. An evident candidate are TEC
422 values as provided via GNSS observations or—more representative for the low Earth orbit—from radar
423 altimetry over the oceans.

424 Conclusions

425 We have implemented a new two-step approach for assimilating along track observations into a physics-
426 based model of the upper atmosphere. First an empirical model is calibrated via scale factors derived
427 from the accelerometer aboard a LEO satellite. In a second step, the calibrated model is evaluated on
428 a regular grid and the resulting neutral densities are assimilated into the numerical model. Here, we
429 use densities derived from the CHAMP accelerometer to calibrate the NRLMSIS 2.0 and assimilate the
430 densities into the TIE-GCM. We applied the approach to a two week long period in 2010 including the
431 5 April 2010 Geomagnetic storm.

432 We demonstrated that the assimilation approach has a global impact on the model and that the model
433 prediction along the CHAMP orbit fits well to the corresponding observations. When comparing the open
434 loop simulation with the assimilation run, the RMSE was reduced from 8.0×10^{-15} to $2.4 \times 10^{-15} \frac{\text{g}}{\text{cm}^3}$.
435 The median difference between model and observations was reduced by two order of magnitudes (7.3^{-15}
436 to $-7.1^{-17} \frac{\text{g}}{\text{cm}^3}$). We believe this approach could be thus beneficial for 'transplanting' the high accuracy
437 of in-situ neutral density observations to other satellites at similar altitudes. It could also be used by
438 modellers to improve the representation of processes and boundary conditions.

439 At altitudes above about 350 km, the density prediction of the model is not improved. For the GRACE
440 satellite basically the sign of the median difference is swapped (open loop simulation: $9.2 \times 10^{-17} \frac{\text{g}}{\text{cm}^3}$
441 assimilation run: $-1.3 \times 10^{-16} \frac{\text{g}}{\text{cm}^3}$). We found that the correction of the first analysis step overshoots
442 the innovation and decreases the model spread at that altitudes. The subsequent analysis steps trust
443 mainly the model forecast and as a results there is a continuous offset between model predictions and
444 observations.

445 We found that during the storm large jumps in the density time series were introduced by the analysis

446 steps. Here, the model moves away fast from the analysed state.

447 We suspect, that both issues can be handled by adding additional entries to the state vector for estimating
448 corrections for TIE-GCM parameters. For example, cooling rates, eddy diffusion, or reaction rates.

449 **Availability of data and materials**

450 The TIE-GCM model code can be downloaded at <https://www.hao.ucar.edu/modeling/tgcm/tie.php>
451 after a registration. The data to run the TIE-GCM is available at [http://download.hao.ucar.edu/
452 pub/tgcm/data/](http://download.hao.ucar.edu/pub/tgcm/data/).

453 The NRLMSIS 2.0 model code is attached to the corresponding publication as supplement (Emmert
454 et al., 2021, Data Set 8) [https://agupubs.onlinelibrary.wiley.com/action/downloadSupplement?
455 doi=10.1029%2F2020EA001321&file=ess2666-sup-0009-2020EA001321-ds08.zip](https://agupubs.onlinelibrary.wiley.com/action/downloadSupplement?doi=10.1029%2F2020EA001321&file=ess2666-sup-0009-2020EA001321-ds08.zip)

456 The code of PDAF can be downloaded <http://pdaf.awi.de/register/index.php> after a registration.

457 The accelerometer derived densities are provided by Vielberg et al. (2021). However, for CHAMP the
458 data sets contains only NaNs in March 2010. The supplement includes a corrected version.

459 The scale factors and the neutral densities (calibrated NRLMSIS 2.0, open loop simulation 3 and
460 assimilation experiment 13) along the GRACE and CHAMP orbit can be found in the supplement of this
461 paper.

462 Please contact the author for the source code of the assimilative version of TIE-GCM or the TIE-GCM
463 output of our experiments on the *state grid* or *data grid*.

464 **Competing interests**

465 None of the authors have competing interest.

466 **Funding**

467 The authors are grateful to the research grant through the TIPOD project (FKZ.: KU 1207/27-1)
468 supported by the German Research Foundation under SPP 1788 (DynamicEarth).

469 **Authors' contributions**

470 AC has integrated PDAF into TIE-GCM, conducted the experiments, created all plots and written large
471 parts of the manuscript. JK helped to refine the draft and contributed to the writing. All authors read

472 and approved the final manuscript.

473 **Acknowledgments**

474 We thank Kristin Vielberg for providing the accelerometer derived neutral densities for CHAMP and
475 GRACE. We would also like to show our gratitude to Lars Nerger for answering many questions about
476 PDAF and Astrid Maute for answering questions about TIE-GCM.

477 **References**

- 478 Bowman, Bruce et al. (2008). “A New Empirical Thermospheric Density Model JB2008 Using New
479 Solar and Geomagnetic Indices”. In: *AIAA/AAS Astrodynamics Specialist Conference and Exhibit*.
480 DOI: 10.2514/6.2008-6438. eprint: <https://arc.aiaa.org/doi/pdf/10.2514/6.2008-6438>.
- 481 Bruinsma, Sean and Claude Boniface (2021). “The Operational and Research DTM-2020 Thermosphere
482 Models”. In: *Journal of Space Weather and Space Climate* 11, p. 47. ISSN: 2115-7251. DOI:
483 10.1051/swsc/2021032.
- 484 Bruinsma, S.L., E. Doornbos, and B.R. Bowman (2014). “Validation of GOCE densities and evaluation
485 of thermosphere models”. In: *Advances in Space Research* 54.4, pp. 576–585. ISSN: 0273-1177. DOI:
486 <https://doi.org/10.1016/j.asr.2014.04.008>. URL:
487 <https://www.sciencedirect.com/science/article/pii/S0273117714002221>.
- 488 Bruinsma, Sean L. et al. (2012). “Evaluation of the DTM-2009 Thermosphere Model for Benchmarking
489 Purposes”. In: *J. Space Weather Space Clim.* 2, A04. DOI: 10.1051/swsc/2012005.
- 490 Codrescu, S. M., M. V. Codrescu, and M. Fedrizzi (2018). “An Ensemble Kalman Filter for the
491 Thermosphere-Ionosphere”. In: *Space Weather* 16.1, pp. 57–68. DOI:
492 <https://doi.org/10.1002/2017SW001752>. eprint:
493 <https://agupubs.onlinelibrary.wiley.com/doi/pdf/10.1002/2017SW001752>. URL:
494 <https://agupubs.onlinelibrary.wiley.com/doi/abs/10.1002/2017SW001752>.
- 495 Doornbos, Eelco (2012). *Thermospheric Density and Wind Determination from Satellite Dynamics*.
496 Springer Theses. Berlin, Heidelberg: Springer Berlin Heidelberg. ISBN: 978-3-642-25128-3
497 978-3-642-25129-0. DOI: 10.1007/978-3-642-25129-0.

498 Drob, D. P. et al. (2008). “An Empirical Model of the Earth’s Horizontal Wind Fields: HWM07”. In:
499 *Journal of Geophysical Research: Space Physics* 113.A12. ISSN: 2156-2202. DOI:
500 10.1029/2008JA013668.

501 Emmert, J. T. (Sept. 2015). “Thermospheric Mass Density: A Review”. In: *Advances in Space Research*
502 56.5, pp. 773–824. ISSN: 0273-1177. DOI: 10.1016/j.asr.2015.05.038.

503 Emmert, J. T. et al. (2021). “NRLMSIS 2.0: A Whole-Atmosphere Empirical Model of Temperature
504 and Neutral Species Densities”. In: *Earth and Space Science* 8.3, e2020EA001321. ISSN: 2333-5084.
505 DOI: 10.1029/2020EA001321.

506 Forootan, Ehsan et al. (Feb. 2022). “Forecasting global and multi-level thermospheric neutral density
507 and ionospheric electron content by tuning models against satellite-based accelerometer
508 measurements”. In: *Scientific Reports* 12, p. 2095. DOI: 10.1038/s41598-022-05952-y. URL:
509 <https://doi.org/10.1038/s41598-022-05952-y>.

510 Gaposchkin, E. M. and A. J. Coster (Jan. 1990). “Evaluation of Thermospheric Models and the
511 Precipitation Index for Satellite Drag”. en. In: *Advances in Space Research* 10.3, pp. 303–309. ISSN:
512 0273-1177. DOI: 10.1016/0273-1177(90)90360-C.

513 Gaspari, Gregory and Stephen E. Cohn (Jan. 1999). “Construction of Correlation Functions in Two and
514 Three Dimensions”. In: *Quarterly Journal of the Royal Meteorological Society* 125.554, pp. 723–757.
515 ISSN: 00359009, 1477870X. DOI: 10.1002/qj.49712555417.

516 Hagan, M. E. and J. M. Forbes (2002). “Migrating and nonmigrating diurnal tides in the middle and
517 upper atmosphere excited by tropospheric latent heat release”. In: *Journal of Geophysical Research:*
518 *Atmospheres* 107.D24, ACL 6–1–ACL 6–15. DOI: <https://doi.org/10.1029/2001JD001236>. eprint:
519 <https://agupubs.onlinelibrary.wiley.com/doi/pdf/10.1029/2001JD001236>. URL:
520 <https://agupubs.onlinelibrary.wiley.com/doi/abs/10.1029/2001JD001236>.

521 Hamill, Thomas M., Jeffrey S. Whitaker, and Chris Snyder (Nov. 2001). “Distance-Dependent Filtering
522 of Background Error Covariance Estimates in an Ensemble Kalman Filter”. In: *Monthly Weather*
523 *Review* 129.11, pp. 2776–2790. ISSN: 1520-0493, 0027-0644. DOI:
524 10.1175/1520-0493(2001)129<2776:DDFOBE>2.0.CO;2.

525 He, Changyong et al. (2018). “Review and comparison of empirical thermospheric mass density
526 models”. In: *Progress in Aerospace Sciences* 103, pp. 31–51. ISSN: 0376-0421. DOI:

527 <https://doi.org/10.1016/j.paerosci.2018.10.003>. URL:

528 <https://www.sciencedirect.com/science/article/pii/S0376042118300629>.

529 Hedin, Alan E. (1987). “MSIS-86 Thermospheric Model”. In: *Journal of Geophysical Research: Space*

530 *Physics* 92.A5, pp. 4649–4662. ISSN: 2156-2202. DOI: 10.1029/JA092iA05p04649.

531 Heelis, R. A., J. K. Lowell, and R. W. Spiro (1982). “A Model of the High-Latitude Ionospheric

532 Convection Pattern”. In: *Journal of Geophysical Research: Space Physics* 87.A8, pp. 6339–6345. ISSN:

533 2156-2202. DOI: 10.1029/JA087iA08p06339.

534 Hunt, Brian R., Eric J. Kostelich, and Istvan Szunyogh (June 2007). “Efficient Data Assimilation for

535 Spatiotemporal Chaos: A Local Ensemble Transform Kalman Filter”. In: *Physica D: Nonlinear*

536 *Phenomena*. Data Assimilation 230.1, pp. 112–126. ISSN: 0167-2789. DOI:

537 10.1016/j.physd.2006.11.008.

538 Jones Jr., M. et al. (2014). “Impacts of Vertically Propagating Tides on the Mean State of the

539 Ionosphere-Thermosphere System”. In: *Journal of Geophysical Research: Space Physics* 119.3,

540 pp. 2197–2213. ISSN: 2169-9402. DOI: 10.1002/2013JA019744.

541 Klinkrad, H. et al. (2006). “Re-Entry Prediction and On-Ground Risk Estimation”. In: *Space Debris:*

542 *Models and Risk Analysis*. Ed. by Heiner Klinkrad. Berlin, Heidelberg: Springer, pp. 241–288. ISBN:

543 978-3-540-37674-3. DOI: 10.1007/3-540-37674-7_9.

544 Lahoz, William, Boris Khattatov, and Richard Menard, eds. (2010). *Data Assimilation: Making Sense*

545 *of Observations*. en. Berlin Heidelberg: Springer-Verlag. ISBN: 978-3-540-74702-4. DOI:

546 10.1007/978-3-540-74703-1.

547 Lee, I. T. et al. (2012). “Assimilation of FORMOSAT-3/COSMIC electron density profiles into a

548 coupled thermosphere/ionosphere model using ensemble Kalman filtering”. In: *Journal of Geophysical*

549 *Research: Space Physics* 117.A10. DOI: <https://doi.org/10.1029/2012JA017700>. eprint:

550 <https://agupubs.onlinelibrary.wiley.com/doi/pdf/10.1029/2012JA017700>. URL:

551 <https://agupubs.onlinelibrary.wiley.com/doi/abs/10.1029/2012JA017700>.

552 Liu, Han-Li et al. (2018). “Development and Validation of the Whole Atmosphere Community Climate

553 Model With Thermosphere and Ionosphere Extension (WACCM-X 2.0)”. In: *Journal of Advances in*

554 *Modeling Earth Systems* 10.2, pp. 381–402. ISSN: 1942-2466. DOI: 10.1002/2017MS001232.

555 Longuski, James M., Felix R. Hoots, and George E. Pollock IV (2022). “Perturbations due to

556 Atmospheric Drag”. In: *Introduction to Orbital Perturbations*. Cham: Springer International

557 Publishing, pp. 277–301. ISBN: 978-3-030-89758-1. DOI: 10.1007/978-3-030-89758-1_12. URL:
558 https://doi.org/10.1007/978-3-030-89758-1_12.

559 Lu, G. et al. (2014). “Global Ionospheric and Thermospheric Response to the 5 April 2010 Geomagnetic
560 Storm: An Integrated Data-Model Investigation”. In: *Journal of Geophysical Research: Space Physics*
561 119.12, pp. 10,358–10,375. ISSN: 2169-9402. DOI: 10.1002/2014JA020555.

562 Matsuo, Tomoko, I-Te Lee, and Jeffrey L. Anderson (2013). “Thermospheric mass density specification
563 using an ensemble Kalman filter”. In: *Journal of Geophysical Research: Space Physics* 118.3,
564 pp. 1339–1350. DOI: <https://doi.org/10.1002/jgra.50162>. eprint:
565 <https://agupubs.onlinelibrary.wiley.com/doi/pdf/10.1002/jgra.50162>. URL:
566 <https://agupubs.onlinelibrary.wiley.com/doi/abs/10.1002/jgra.50162>.

567 Matzka, J. et al. (2021). “The Geomagnetic Kp Index and Derived Indices of Geomagnetic Activity”.
568 In: *Space Weather* 19.5, e2020SW002641. ISSN: 1542-7390. DOI: 10.1029/2020SW002641.

569 Montenbruck, Oliver and Eberhard Gill (2005). *Satellite orbits: models, methods and applications*. Corr.,
570 3.print. Berlin u.a.: Springer. ISBN: 354067280X, 9783540672807. DOI: 10.1007/978-3-642-58351-3.

571 Morozov, Alexey V. et al. (2013). “Data assimilation and driver estimation for the Global
572 Ionosphere–Thermosphere Model using the Ensemble Adjustment Kalman Filter”. In: *Journal of*
573 *Atmospheric and Solar-Terrestrial Physics* 104, pp. 126–136. ISSN: 1364-6826. DOI:
574 <https://doi.org/10.1016/j.jastp.2013.08.016>. URL:
575 <https://www.sciencedirect.com/science/article/pii/S1364682613002289>.

576 Nerger, Lars, Qi Tang, and Longjiang Mu (Sept. 2020). “Efficient Ensemble Data Assimilation for
577 Coupled Models with the Parallel Data Assimilation Framework: Example of AWI-CM
578 (AWI-CM-PDAF 1.0)”. In: *Geoscientific Model Development* 13.9, pp. 4305–4321. ISSN: 1991-959X.
579 DOI: 10.5194/gmd-13-4305-2020.

580 Nerger, Lars et al. (Dec. 2006). “Using Sea-Level Data to Constrain a Finite-Element
581 Primitive-Equation Ocean Model with a Local SEIK Filter”. In: *Ocean Dynamics* 56.5, pp. 634–649.
582 ISSN: 1616-7228. DOI: 10.1007/s10236-006-0083-0.

583 Nerger, Lars et al. (2012a). “A Regulated Localization Scheme for Ensemble-Based Kalman Filters”. In:
584 *Quarterly Journal of the Royal Meteorological Society* 138.664, pp. 802–812. ISSN: 1477-870X. DOI:
585 10.1002/qj.945.

586 Nerger, Lars et al. (2012b). “A Unification of Ensemble Square Root Kalman Filters”. In: *Monthly*
587 *Weather Review* 140.7, pp. 2335–2345. DOI: 10.1175/MWR-D-11-00102.1. eprint:
588 <https://doi.org/10.1175/MWR-D-11-00102.1>.

589 Panzetta, Francesca et al. (Mar. 2019). “Towards Thermospheric Density Estimation from SLR
590 Observations of LEO Satellites: A Case Study with ANDE-Pollux Satellite”. en. In: *J Geod* 93.3,
591 pp. 353–368. ISSN: 1432-1394. DOI: 10.1007/s00190-018-1165-8.

592 Papitashvili, Natalia E. and Joseph H King (2020). *OMNI 1-min Data*. DOI:
593 <https://doi.org/10.48322/45bb-8792>.

594 Picone, J. M. et al. (2002). “NRLMSISE-00 Empirical Model of the Atmosphere: Statistical
595 Comparisons and Scientific Issues”. In: *Journal of Geophysical Research: Space Physics* 107.A12, SIA
596 15–1–SIA 15–16. DOI: 10.1029/2002JA009430. eprint:
597 <https://agupubs.onlinelibrary.wiley.com/doi/pdf/10.1029/2002JA009430>.

598 Qian, Liying et al. (2014). “The NCAR TIE-GCM: A Community Model of the Coupled
599 Thermosphere/Ionosphere System”. In: *Modeling the Ionosphere–Thermosphere System*. Ed. by
600 Joseph Huba, Robert Schunk, and Khazanov George. First. Geophysical Monograph Series. American
601 Geophysical Union (AGU), pp. 73–83. DOI: 10.1002/9781118704417. eprint:
602 <https://agupubs.onlinelibrary.wiley.com/doi/pdf/10.1002/9781118704417>.

603 Reigber, Ch., H. Lühr, and P. Schwintzer (2002). “CHAMP mission status”. In: *Advances in Space*
604 *Research* 30.2, pp. 129–134. ISSN: 0273-1177. DOI:
605 [https://doi.org/10.1016/S0273-1177\(02\)00276-4](https://doi.org/10.1016/S0273-1177(02)00276-4). URL:
606 <https://www.sciencedirect.com/science/article/pii/S0273117702002764>.

607 Richards, P. G., J. A. Fennelly, and D. G. Torr (1994). “EUVAC: A Solar EUV Flux Model for
608 Aeronomic Calculations”. In: *Journal of Geophysical Research: Space Physics* 99.A5, pp. 8981–8992.
609 ISSN: 2156-2202. DOI: 10.1029/94JA00518.

610 Ridley, A. J., Y. Deng, and G. Tóth (May 2006). “The Global Ionosphere–Thermosphere Model”. In:
611 *Journal of Atmospheric and Solar–Terrestrial Physics* 68.8, pp. 839–864. ISSN: 1364-6826. DOI:
612 [10.1016/j.jastp.2006.01.008](https://doi.org/10.1016/j.jastp.2006.01.008).

613 Sheng, Cheng et al. (2017). “Thermospheric Recovery during the 5 April 2010 Geomagnetic Storm”. In:
614 *Journal of Geophysical Research: Space Physics* 122.4, pp. 4588–4599. ISSN: 2169-9402. DOI:
615 [10.1002/2016JA023520](https://doi.org/10.1002/2016JA023520).

616 Solomentsev, D. V. et al. (2012). “Ionosphere state and parameter estimation using the Ensemble
617 Square Root Filter and the global three-dimensional first-principle model”. In: *Space Weather* 10.7.
618 DOI: <https://doi.org/10.1029/2012SW000777>. eprint:
619 <https://agupubs.onlinelibrary.wiley.com/doi/pdf/10.1029/2012SW000777>. URL:
620 <https://agupubs.onlinelibrary.wiley.com/doi/abs/10.1029/2012SW000777>.

621 Tapley, Byron D. et al. (2007). “Neutral Density Measurements from the Gravity Recovery and Climate
622 Experiment Accelerometers”. In: *Journal of Spacecraft and Rockets* 44.6, pp. 1220–1225. DOI:
623 10.2514/1.28843. eprint: <https://doi.org/10.2514/1.28843>. URL:
624 <https://doi.org/10.2514/1.28843>.

625 Tapping, K. F. (2013). “The 10.7 cm solar radio flux (F10.7)”. In: *Space Weather* 11.7, pp. 394–406.
626 DOI: <https://doi.org/10.1002/swe.20064>. eprint:
627 <https://agupubs.onlinelibrary.wiley.com/doi/pdf/10.1002/swe.20064>. URL:
628 <https://agupubs.onlinelibrary.wiley.com/doi/abs/10.1002/swe.20064>.

629 Vallado, David A. and David Finkleman (Feb. 2014). “A Critical Assessment of Satellite Drag and
630 Atmospheric Density Modeling”. In: *Acta Astronautica* 95, pp. 141–165. ISSN: 0094-5765. DOI:
631 10.1016/j.actaastro.2013.10.005.

632 Vetra-Carvalho, Sanita et al. (2018). “State-of-the-art stochastic data assimilation methods for
633 high-dimensional non-Gaussian problems”. In: *Tellus A: Dynamic Meteorology and Oceanography*
634 70.1, pp. 1–43. DOI: 10.1080/16000870.2018.1445364. eprint:
635 <https://doi.org/10.1080/16000870.2018.1445364>. URL:
636 <https://doi.org/10.1080/16000870.2018.1445364>.

637 Vielberg, K. et al. (2018). “Comparison of Accelerometer Data Calibration Methods Used in
638 Thermospheric Neutral Density Estimation”. In: *Annales Geophysicae* 36.3, pp. 761–779. DOI:
639 10.5194/angeo-36-761-2018.

640 Vielberg, Kristin and Jürgen Kusche (Mar. 2020). “Extended Forward and Inverse Modeling of
641 Radiation Pressure Accelerations for LEO Satellites”. In: *Journal of Geodesy* 94.4, p. 43. ISSN:
642 1432-1394. DOI: 10.1007/s00190-020-01368-6.

643 Vielberg, Kristin et al. (2021). *TND-IGG RL01: Thermospheric neutral density from accelerometer*
644 *measurements of GRACE, CHAMP and Swarm*. data set. DOI: 10.1594/PANGAEA.931347. URL:
645 <https://doi.org/10.1594/PANGAEA.931347>.

646 Walterscheid, R. L. (Nov. 1989). “Solar Cycle Effects on the Upper Atmosphere - Implications for
647 Satellite Drag”. In: *Journal of Spacecraft and Rockets* 26.6, pp. 439–444. ISSN: 0022-4650, 1533-6794.
648 DOI: 10.2514/3.26089.

649 Weimer, D. R. (2005). “Improved Ionospheric Electrodynamic Models and Application to Calculating
650 Joule Heating Rates”. In: *Journal of Geophysical Research: Space Physics* 110.A5. ISSN: 2156-2202.
651 DOI: 10.1029/2004JA010884.

652 Zeitler, Lea et al. (2021). “Scale Factors of the Thermospheric Density: A Comparison of Satellite Laser
653 Ranging and Accelerometer Solutions”. In: *Journal of Geophysical Research: Space Physics* 126.12,
654 e2021JA029708. ISSN: 2169-9402. DOI: 10.1029/2021JA029708.

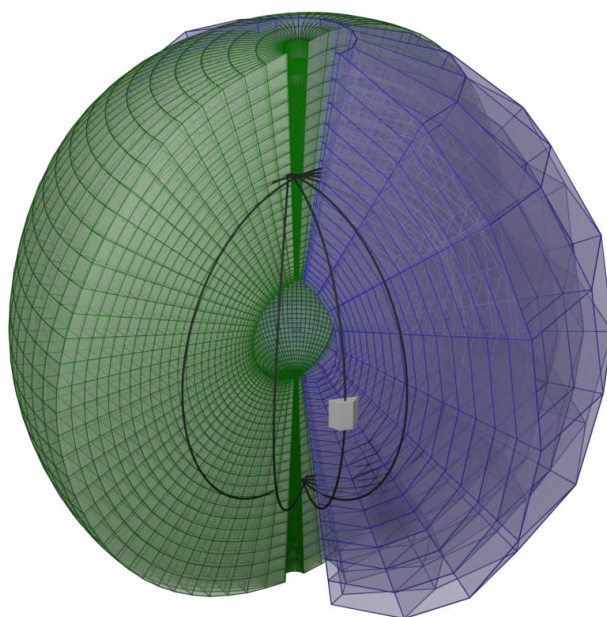


Figure 1. The green lines illustrate the grid of the TIE-GCM at one epoch. We call it the *state grid*. The blue lines show the (constant) grid at which we evaluate the NRLMSIS 2.0. We call it the *data grid*. The black curve illustrates the orbit of the CHAMP satellite for some revolutions. In the two-step approach we first calibrate the NRLMSIS 2.0 with the accelerometer derived density of the CHAMP satellite, and evaluate it on the *data grid*. In a second step we assimilated the densities located on the *data grid*—in data assimilation terminology this are the observations—into the TIE-GCM. The grids appear thicker as they are in reality, since the radius of Earth is not added. Actually both grids cover the entire Earth, but we show only a subset for a clearer illustration.

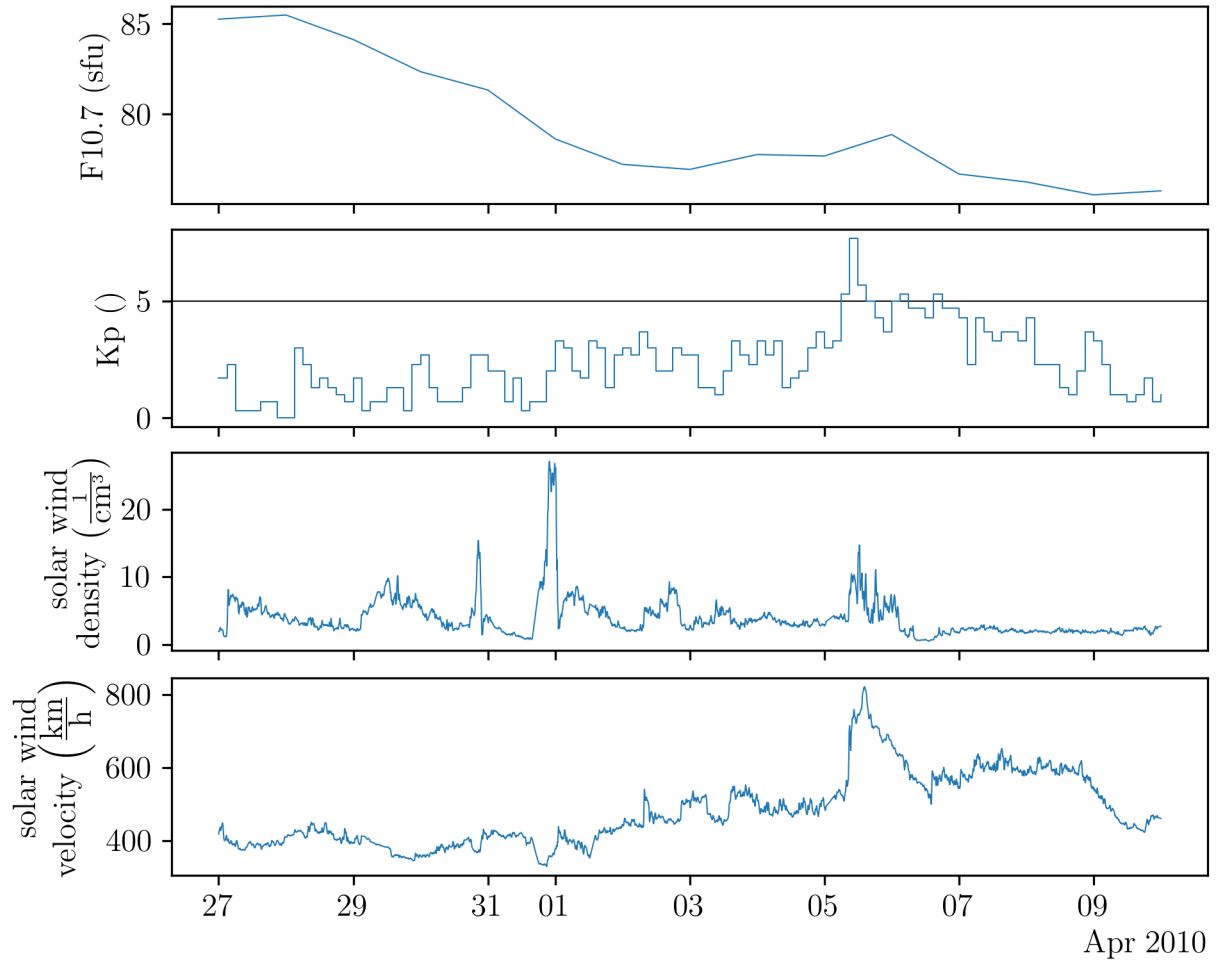


Figure 2. External forcing time series during the period of the experiment required to run the NRLMSIS 2.0 and TIE-GCM. A Kp value greater than or equal to five is considered as storm. The main storm event is at 5th April from 6:00 to 18:00 UTC+0. The temporal resolution of the F10.7 index, Kp index and the OMNI solar wind parameters is one day, three hours and one minute, respectively.

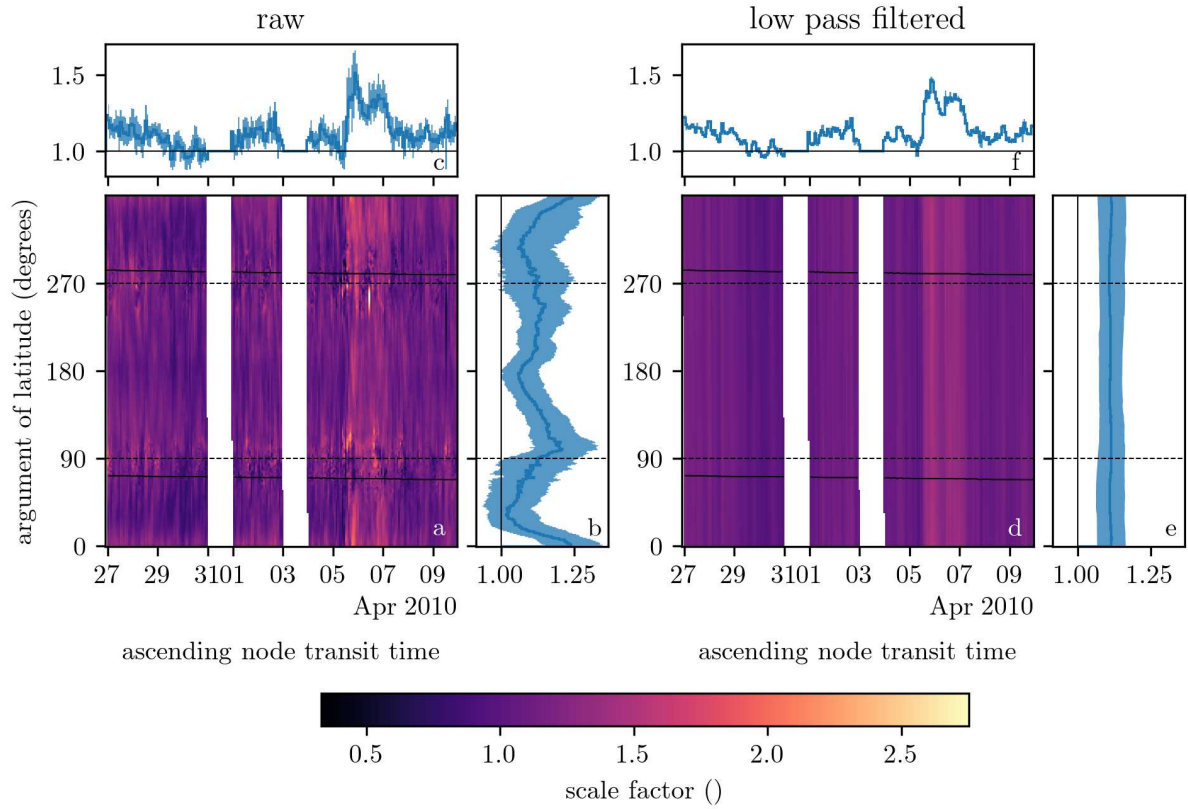


Figure 3. Panel a shows the scale factor between the neutral densities computed with NRLMSIS 2.0 and the neutral densities derived from the CHAMP accelerometer. The argument of latitude is the angle—measured on the orbital plane—between the ascending node and the satellite. Values of 0° and 180° correspond to the night side and day side equator, respectively. At 90° and 270° CHAMP is closest the north and south pole, respectively. The solid black line is the border between day and night side. The dashed black line marks the point where the satellite is closest to the poles. The solid blue line in panel b is the median scale factor at the corresponding argument of latitude. The solid blue line in panel c is the median scale factor at the corresponding orbit. The light blue areas in panel b and c mark the interval between the 25th and 75th percentile. Panels d,e,f show the scale factors filtered with a three hourly low pass filter analogously to panels a,b,c.

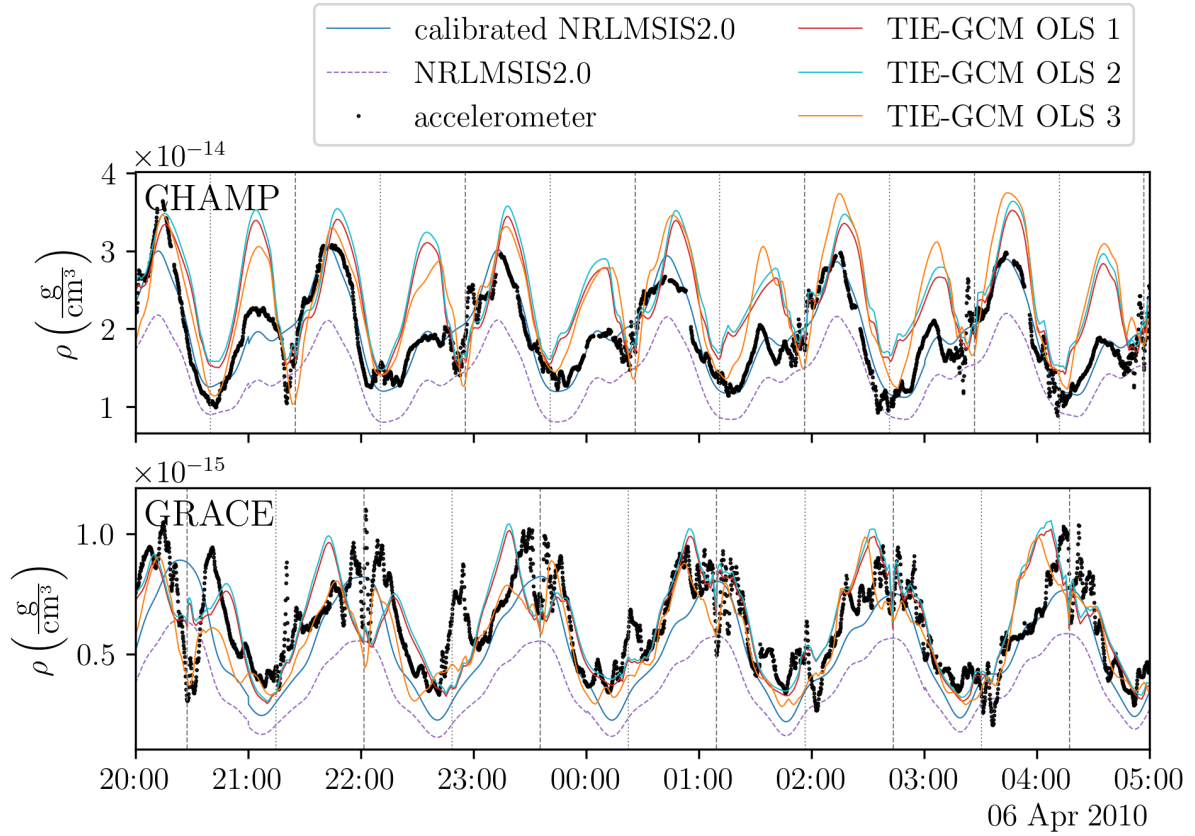


Figure 4. The neutral mass density along the orbits of CHAMP and GRACE is plotted for a nine hour long period. The dashed vertical gray lines indicate the transits above the north pole and the dotted vertical gray lines the transits above the south pole. The calibrated NRLMSIS 2.0 time series was computed using scale factors filtered with a cut-off frequency of eight cpd

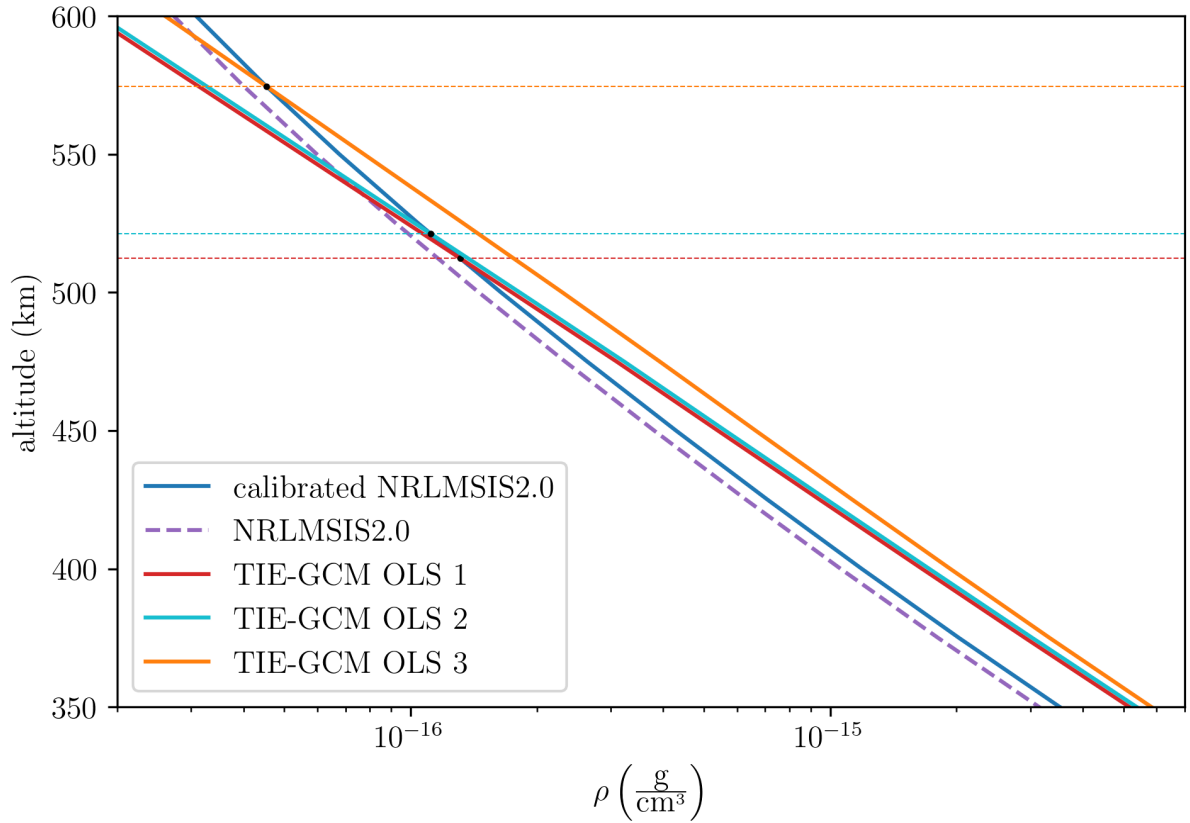


Figure 5. For each altitude of the *data grid* we computed the median of the neutral mass density including all longitudes, latitudes and times. The horizontal dotted lines indicate the intersection of the height profile of the NRLMSIS 2.0 with the profile of the corresponding open loop simulation. Below 350 km the lines do not intersect.

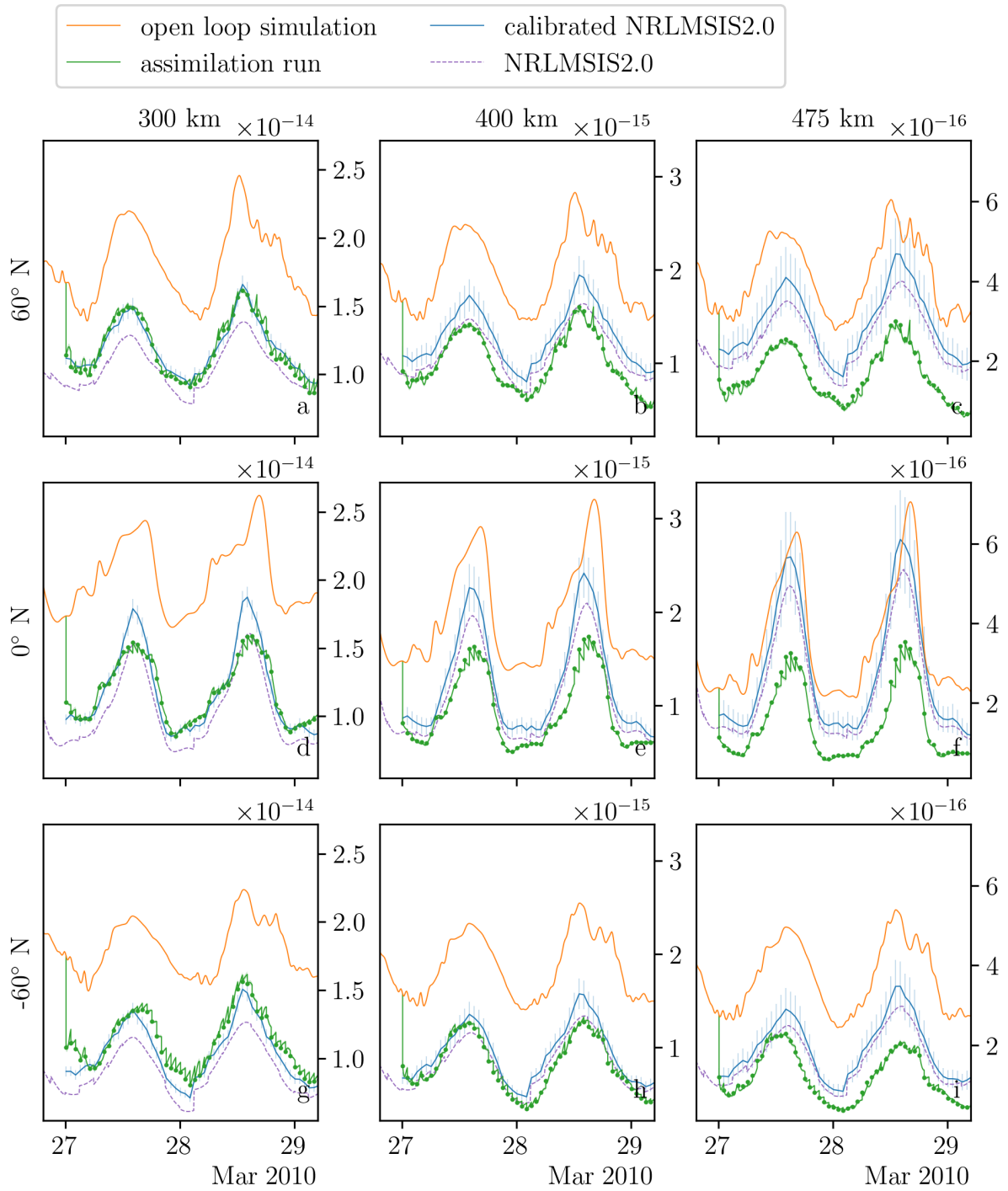


Figure 6. Each panel contains time series of neutral density ($\frac{n_e}{\text{cm}^3}$) for different cells of the *data grid*. Each row corresponds to a geocentric latitude and each column to an ellipsoidal height. The longitude is always $0^\circ E$. The panels of each column share the same y-axis. The errors bands or bars show the standard deviation. This figure shows the first two days of the experiment with quiet geomagnetic conditions.

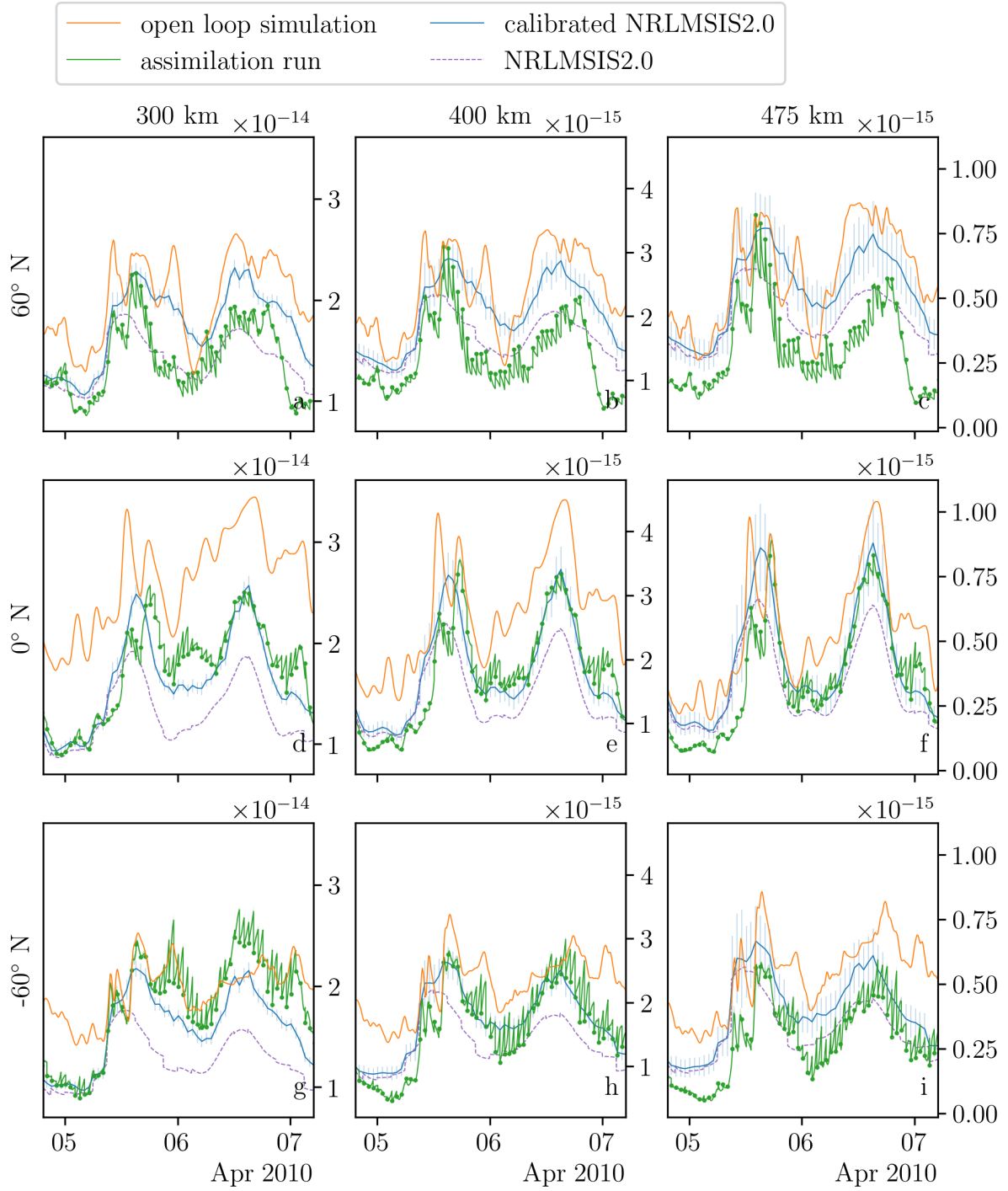


Figure 7. Each panel contains time series of neutral density ($\frac{g}{cm^3}$) for different cells of the *data grid*. Each row corresponds to a geocentric latitude and each column to an ellipsoidal height. The longitude is always $0^\circ E$. The panels of each column share the same y-axis. The errors bands or bars show the standard deviation. This figure shows two days of the experiment including the storm at 5th April.

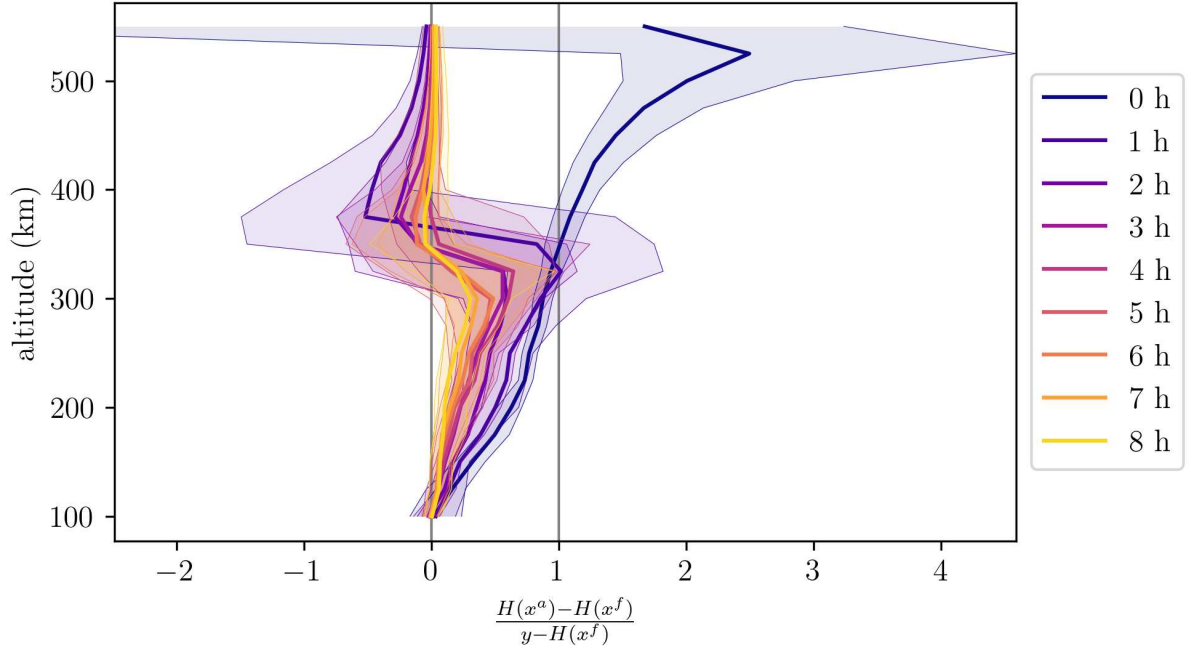


Figure 8. This height profile illustrates the average ratio of the analysed ($y - H(x^a)$) and forecasted ($y - H(x^f)$) observational residuals for the first nine analysis steps. For easier interpretation we subtract the ratio from one: $\frac{H(x^a) - H(x^f)}{y - H(x^f)} = 1 - \frac{y - H(x^a)}{y - H(x^f)}$. A value of zero means that observations have no impact and the analysed state is equal to the forecasted state. A value of one means that the full innovation is adopted. Negative values mean the analysed state (transformed to the observation space) is pushed away from the observations. The solid bold line is the median computed over all layers of the *data grid* at the corresponding color coded analysis step. The shaded area marks the interval between the 25th and 75th percentile. Here x^a is the analyzed state after applying constraints.

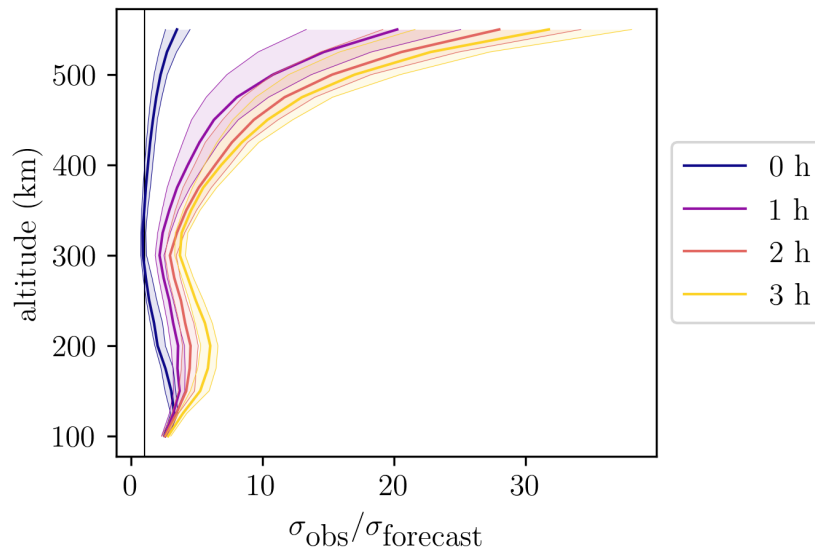


Figure 9. For the first four analysis steps, the average ratio of the standard deviation of the NRLMSIS 2.0, and the model forecast are plotted for each level of the *data grid*. A value of one means that both have the same uncertainty. Values greater than one indicate that the observation error is larger than the forecast error. The solid solid line is the median computed over all layers of the *data grid* at the corresponding color coded analysis step. The shaded area marks the interval between the 25th and 75th percentile.

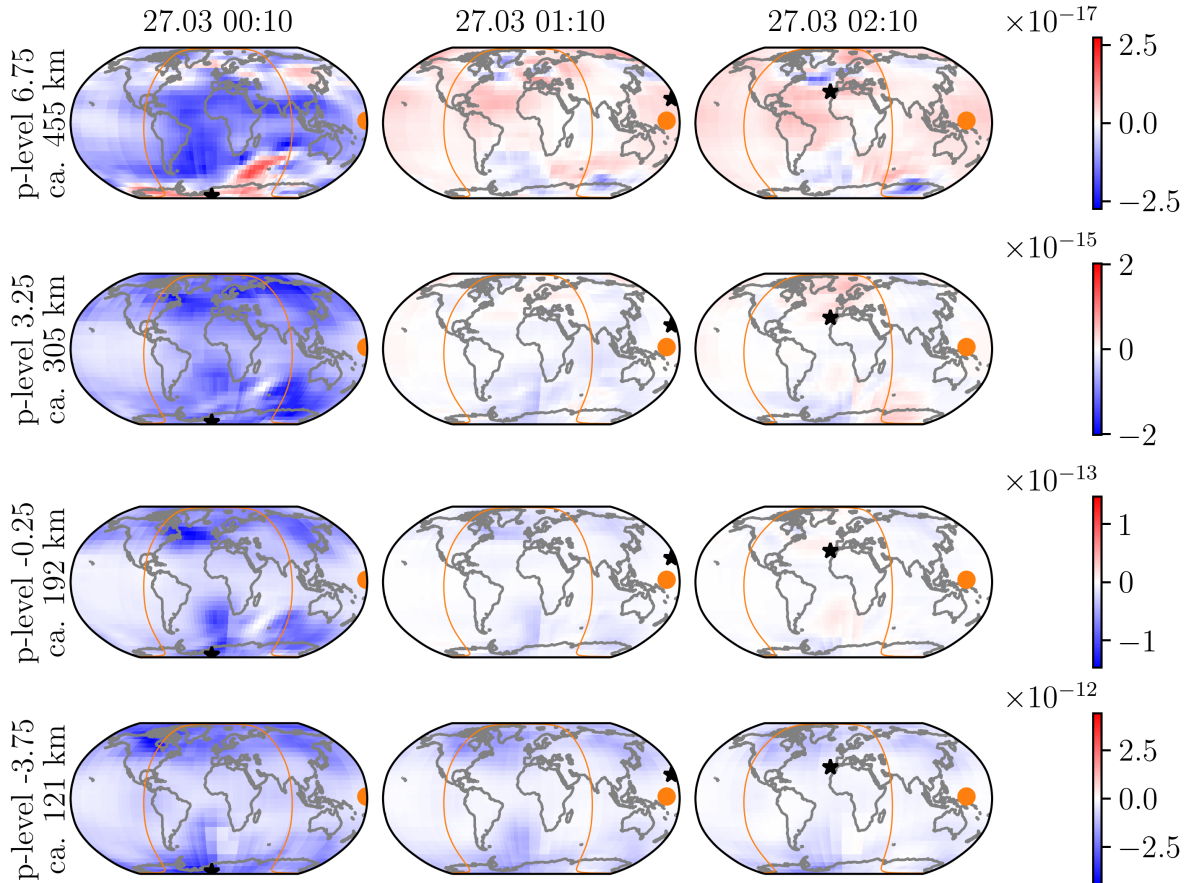


Figure 10. Each map corresponds to a pressure level of the *state grid*. The difference between the forecast mean and analysis mean of the neutral density ($\frac{g}{cm^3}$) is indicated by the color bars on the right. Each row corresponds to a pressure level. each column to an analysis step. This figure shows the three first update steps. The horizontal position of CHAMP is marked with a black star, the position of the Sun with an orange circle, and the day night border with an orange line.

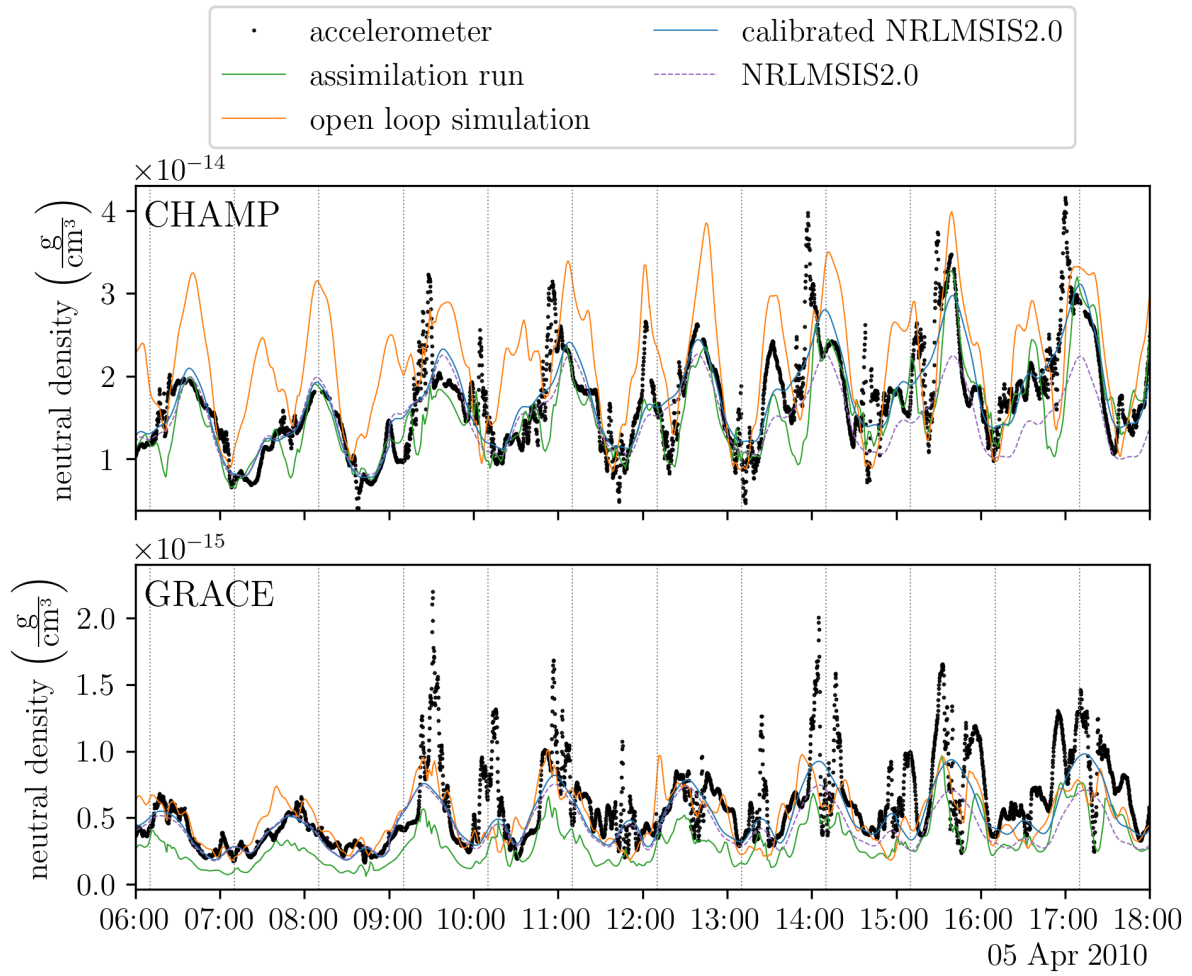


Figure 11. Densities along the orbits of CHAMP and GRACE from various sources. The x axis is limited to a period where KP is always larger than or equal to 5 and contains the largest KP value of $7\frac{2}{3}$ in the experiment (9:00-12:00). The dotted vertical lines mark the analysis steps.

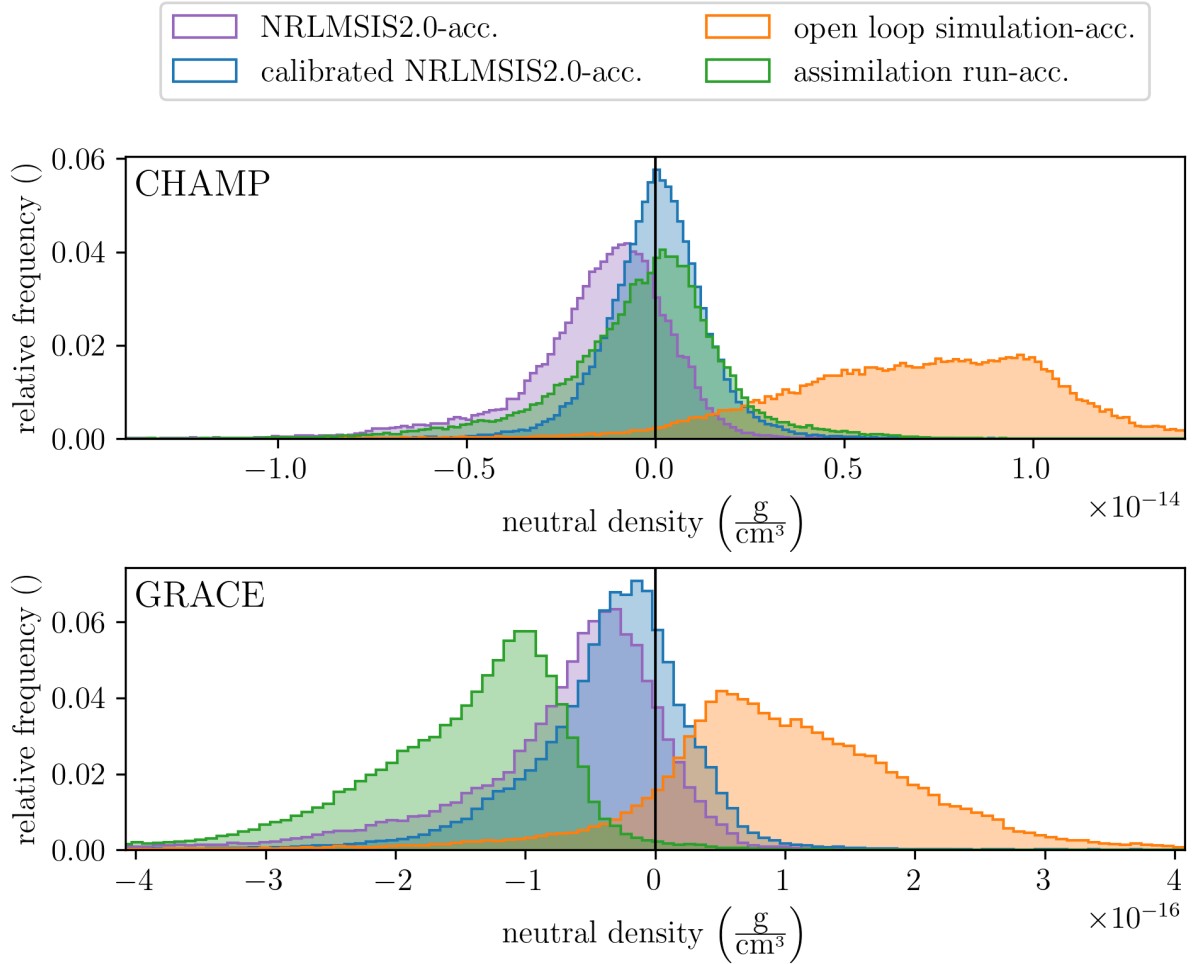


Figure 12. The densities along the GRACE and CHAMP orbit were interpolated from the assimilated TIE-GCM and the open loop simulation. Additionally the (calibrated) NRLMSIS 2.0 was evaluated along the corresponding orbits. This figure shows the histograms of these three time series reduced by the accelerometer derived densities.

Supplementary Files

This is a list of supplementary files associated with this preprint. Click to download.

- [champTNDIGGRL01201003.nc](#)
- [champTNDIGGRL01201004.nc](#)
- [champassimilationexperiment13.nc](#)
- [champcalibratedNRLMSIS2.nc](#)
- [champopenloopsimulation3.nc](#)
- [graceTNDIGGRL01201003.nc](#)
- [graceTNDIGGRL01201004.nc](#)
- [graceassimilationexperiment13.nc](#)
- [gracecalibratedNRLMSIS2.nc](#)
- [graceopenloopsimulation3.nc](#)
- [graphicalabstract.png](#)